

Full one-loop radiative corrections to $e^+e^- \rightarrow H^+H^-$ in the inert doublet model

Hamza Abouabid^{1*}, Abdesslam Arhrib^{1†}, Jaouad El Falaki^{2‡}, Bin Gong^{3,4§},
Wenhai Xie^{3,4¶}, Qi-Shu Yan^{4,5||},

¹ *Université Abdelmalek Essaadi, FSTT, B. 416, Tangier, Morocco.*

² *LPTHE, Physics Department, Faculty of Sciences, Ibnou Zohr University, P.O.B. 8106 Agadir, Morocco.*

³ *Theory Division, Institute of High Energy Physics, Chinese Academy of Sciences, Beijing 100049, China.*

⁴ *School of Physics Sciences, University of Chinese Academy of Sciences, Beijing 100049, China.*

⁵ *Center for Future High Energy Physics, Chinese Academy of Sciences, Beijing 100049, China.*

Abstract

We compute the full one-loop radiative corrections for charged scalar pair production $e^+e^- \rightarrow H^+H^-$ in the inert doublet model. The on-shell renormalization scheme has been used. We take into account both the weak contributions as well as the soft and hard QED corrections. We compute both the real emission and the one-loop virtual corrections using the Feynman diagrammatic method. The resummed cross section is introduced to cure the Coulomb singularity which occurs in the QED corrections. We have analyzed the parameter space of the inert doublet model in three scenarios after taking into account theoretical constraints, the collider experimental bounds, and dark matter search bounds as well. It is found that the weak interaction dominates the radiative corrections, and its size is determined by the triple Higgs coupling $\lambda_{h^0 H^+ H^-}$, which is further connected to the mass of the charged scalar. In the scenario where all the constraints are taken into account, we find that for $\sqrt{s} = 250$ GeV and $\sqrt{s} = 500$ GeV, the weak corrections are around $-6\% \sim -5\%$ and $-10\% \sim -3\%$, respectively. While for $\sqrt{s} = 1000$ GeV, the weak corrections can reach $-15\% \sim +25\%$. The new feature is that the weak corrections can be positive near the threshold when the charged scalar is heavier than 470 GeV. Six benchmark points for future collider searches have been proposed.

*E-mail: hamza.abouabid@gmail.com

†E-mail: aarhrib@gmail.com

‡E-mail: jaouad.elfalaki@gmail.com

§E-mail: twain@ihep.ac.cn

¶E-mail: xiewh@ihep.ac.cn

||E-mail: yanqishu@ucas.ac.cn

1 Introduction

The Standard Model (SM) particle spectrum has been completed with the discovery of the Higgs boson on July 4, 2012, by the ATLAS and CMS experiments at CERN [1, 2]. Furthermore, this discovery has confirmed that the SM of particle physics is the underlying theoretical framework valid at least for energies up to the electroweak (EW) scale. The two collaborations also carried out several Higgs boson couplings measurements at the Large Hadron Collider (LHC) during run-1 and run-2 such as the couplings of the Higgs boson to top quarks [3, 4], tau leptons [5, 6], bottom quarks [7, 8], and all the electroweak gauge bosons, including the decays to ZZ^* [9, 10], WW^* [11–14], and $\gamma\gamma$ [15]. In addition, recently upper limits have been set on the $h^0 \rightarrow \gamma Z$ signal strength [16, 17] and on the Higgs boson production cross section times branching fraction to muons [18, 19].

The aforementioned measurements will be improved at future experiments such as the High-Luminosity LHC [20, 21], scheduled to operate from 2029, where the Higgs boson couplings are projected to be improved to a precision level of 5 – 10%. In addition, the experimental uncertainties will be further reduced in the clean environment of the future lepton colliders, such as the International Linear Collider (ILC) [22, 23], the Circular Electron Positron Collider (CEPC) [24], the Compact Linear Collider (CLIC) [25–27], and the Future Circular Collider [28]. For example, at the ILC, with a c.m.energy of about 250 GeV and a luminosity of 2 ab^{-1} , some Higgs boson couplings will most likely be measured at a precision level of 1% for $h^0 \rightarrow b\bar{b}$ and below 1% for $h^0 \rightarrow ZZ, WW$ [29].

Although new physics beyond the SM has not yet been established by the current LHC dataset, it is necessary in order to understand several puzzles of the SM and the observed Universe, such as what is the nature of dark matter, what is the origin of neutrino masses, how to stabilize the vacuum of the SM, and so on. From the viewpoint of effective theory, the success of the SM can only be understood as the low energy limit of a more fundamental theory. In this more fundamental theory, there must be extra sectors not included by the SM. For example, the Higgs sector of the SM is assumed to be minimal and composed of only one Higgs doublet. In order to solve the problem of CP violation, it is well motivated to extend the Higgs sector of the SM by introducing one more doublet [30] and the Higgs potential sector can be extended, such a theory model is called the two Higgs doublet model (2HDM). A comprehensive review of the 2HDM can be found in the reference [31].

In order to offer a dark matter candidate, a \mathbb{Z}_2 symmetry is introduced into the 2HDM, which leads to the so-called inert doublet model (IDM). In the IDM, the second doublet does not develop a vacuum expectation value (VEV) nor does it have a direct coupling to the SM fermions. In such a \mathbb{Z}_2 symmetry, the fermions, gauge bosons, and the SM Higgs doublet are invariant, and the second doublet is odd, i.e. $H_2 \rightarrow -H_2$. The \mathbb{Z}_2 symmetry ensures that this extra doublet has no direct coupling to the SM fermions at both tree and loop levels, and its lightest stable neutral component may play the role of a dark matter candidate. The IDM was proposed by E. Ma et al. [32] and it was initially suggested for studies on electroweak symmetry breaking. This model is very appealing because it can generate small neutrino masses [33], can provide a dark matter candidate [34–40] and can solve the naturalness problem [41]. The phenomenology of the IDM has been extensively studied in the literature in the context of the LHC and at future Higgs factories such as the ILC or CLIC [42–80].

After the electroweak symmetry breaking, the IDM possesses five physical scalars: One Higgs boson h^0 which is identified as the 125 GeV SM Higgs, two new neutral physical scalars H^0 , A^0 and two charged physical scalars H^\pm . Both H^0 and A^0 could be dark matter candidates.

Obviously, the discovery of a charged scalar boson would be a clear sign of nonminimal Higgs sectors and precise knowledge of its production properties would be useful to reconstruct the full Higgs potential. Since all new IDM scalars are odd under the \mathbb{Z}_2 symmetry, they must be produced in pairs at the colliders. Moreover, these new inert scalars only couple to the electroweak gauge bosons and the Higgs boson of the SM. Consequently, at the LHC they should be pair-produced via processes of the Drell-Yan type: $q\bar{q}' \rightarrow W^* \rightarrow A^0 H^\pm$, $q\bar{q}' \rightarrow W^* \rightarrow H^0 H^\pm$, and $q\bar{q} \rightarrow Z^*(\gamma) \rightarrow H^+ H^-$, or from $gg, q\bar{q} \rightarrow h^{0*} \rightarrow H^+ H^-$ [53, 72], where \bar{q}' represents a different quark flavor. Furthermore, the charged scalars in the IDM could also be produced in the same-sign pair production process $pp \rightarrow H^\pm H^\pm jj$ [52, 81, 82] or from vector boson fusion-like production $pp \rightarrow H^\pm H^\mp jj$ [53]. At lepton colliders, charged scalars can be produced via the pair production process $e^+ e^- \rightarrow H^+ H^-$ [43, 49, 50]. Future muon colliders [83, 84] may have better potential to cover a wide range of the mass of charged scalars.

The discovery of a charged scalar would be clear evidence of beyond the SM physics. In the case such a discovery happens in $e^+ e^-$ collider, a subsequent precision measurement of its properties will be crucial to determine its nature. In order to obtain sufficient accuracy, one-loop corrections to the various charged scalar production modes and its couplings have to be considered. Recently, one loop radiative corrections to $e^+ e^- \rightarrow Zh^0$ [85–87] and $e^+ e^- \rightarrow H^0 A^0$ [85] in the IDM have been evaluated. In addition, there are many other works dealing with radiative corrections in the IDM either at one-loop order [85–96] or beyond the one-loop level [97–99]. Full one-loop calculations to $e^+ e^- \rightarrow H^+ H^-$ in nonsupersymmetric models such as the 2HDM and some supersymmetric models like the real minimal supersymmetric standard model (MSSM) and complex MSSM have been presented in Refs [100–107]. For example, it has been found in the complex MSSM [107] that radiative corrections to $e^+ e^- \rightarrow H^+ H^-$ can go up to 20% or higher, hence a full one-loop contributions are important for future linear colliders such as the ILC or CLIC.

In this work, we present for the first time a full one-loop analysis to $e^+ e^- \rightarrow H^+ H^-$ within the IDM. Besides the full weak corrections, we include the soft and hard QED radiation as well as the treatment of collinear divergences and the Coulomb singularity. In our scan and numerical analysis, we will take into account all the existing constraints on the IDM including the theoretical ones, the experimental constraints from the LHC, such as the Higgs data from the decay of the Higgs boson into two photons, the invisible Higgs decay, the electroweak precision tests, as well as the constraints from dark matter relic density in the Universe and the direct bounds from the monojet searches at the LHC. It should be mentioned that we have included the recast results from LEP II data [108] in our scan and analysis. Additional LHC recast results, such as dilepton and multilepton final states, as well as vector boson fusion final states, can be found in Refs. [62, 63, 109, 110]. These recasts might bring new limits to the IDM parameter space. However, in this work, they are not taken into consideration.

We perform a scan over the whole parameter space of the IDM in three scenarios: Scenario I assumes that the inert scalars are degenerate in mass and has taken into account all the constraints except the invisible Higgs decay and dark matter constraints, scenario II is defined by imposing all the constraints without dark matter ones and with a nondegenerate spectrum for the new inert scalars and scenario III is the same as scenario II but with dark matter constraints. We find that the dark matter constraints can greatly reduce the number of points in the parameter space. Furthermore, it is found that QED corrections are rather small and radiative corrections are dominated by the weak interactions. The size of weak corrections depends on the coupling $\lambda_{h^0 H^+ H^-}$, which is further related to the mass of charged scalar. In scenario III we find that for $\sqrt{s} = 250$ and $\sqrt{s} = 500$ GeV, the weak corrections are around

$-6\% \sim -5\%$ and $-10\% \sim -3\%$, respectively. While for $\sqrt{s} = 1000$ GeV, the weak corrections can reach $-15\% \sim +25\%$. The new feature is that the weak corrections can be positive near the threshold when the charged scalar mass is larger than 470 GeV. We have proposed six benchmark points for future lepton collider searches.

The outline of this paper is as follows: In Sec. 2, we briefly describe the model, including its mass spectra, key trilinear and quartic scalar couplings, and list various theoretical and experimental constraints that we will take into account in this work. In Sec. 3, we provide the leading-order (LO) formula for the cross sections of the $e^+e^- \rightarrow H^+H^-$ process, introduce the on-shell renormalization scheme for the IDM, and set up basic notations and conventions. Moving on, we study the one-loop contributions to the $e^+e^- \rightarrow H^+H^-$ process and examine the importance of soft and hard photon emission in order to guarantee the cancellation of the infrared (IR) divergences at the next-to-leading order (NLO) calculation. Furthermore, we tackle the challenge posed by the Coulomb singularity using efficient resummation techniques. We present our numerical results in Sec. 4. In Sec. 5, we propose some benchmark points (BPs) and examine their radiative corrections for future e^+e^- colliders. We end this work with discussions in Sec. 6.

2 Review of the inert doublet model

2.1 A brief introduction to IDM

The IDM is one of the simplest extensions beyond the SM. This model has an extra doublet H_2 which is added to the scalar sector of the SM. This doublet does not generate any VEV and it does not have direct coupling to the fermions of the SM. An unbroken \mathbb{Z}_2 symmetry is imposed such that fermions, gauge bosons, and the SM doublet are invariant while the additional scalar doublet is odd i.e. $H_2 \rightarrow -H_2$ under this symmetry. The parametrization of the two doublets is given by

$$H_1 = \begin{pmatrix} G^\pm \\ \frac{1}{\sqrt{2}}(v + h^0 + iG^0) \end{pmatrix}, \quad H_2 = \begin{pmatrix} H^\pm \\ \frac{1}{\sqrt{2}}(H^0 + iA^0) \end{pmatrix}, \quad (1)$$

where G^0 and G^\pm are the Goldstone bosons gauged out, after electroweak symmetry breaking, by the longitudinal components of W^\pm and Z , respectively. The v denotes the VEV of the SM Higgs doublet H_1 .

Then the renormalizable scalar potential can be given as:

$$\begin{aligned} V = & \mu_1^2 |H_1|^2 + \mu_2^2 |H_2|^2 + \lambda_1 |H_1|^4 + \lambda_2 |H_2|^4 + \lambda_3 |H_1|^2 |H_2|^2 + \lambda_4 |H_1^\dagger H_2|^2 \\ & + \frac{\lambda_5}{2} \left\{ (H_1^\dagger H_2)^2 + \text{H.c.} \right\}. \end{aligned} \quad (2)$$

Note that because of the exact \mathbb{Z}_2 symmetry, the above potential has no mixing terms like $\mu_{12}^2 (H_1^\dagger H_2 + \text{H.c.})$. In addition, since the potential must be Hermitian, all $\lambda_i, i = 1, \dots, 4$ are dimensionless and real whilst the phase of λ_5 can be absorbed by a suitable redefinition of the fields H_1 and H_2 . After spontaneous symmetry breaking of the group $SU(2)_L \otimes U(1)_Y$ down to $U(1)_{em}$, we have five physical scalars: h^0 which is the SM 125 GeV Higgs boson and four inert scalars: H, A, H^\pm . Their masses are given by:

$$\begin{aligned} m_{h^0}^2 &= -2\mu_1^2 = 2\lambda_1 v^2 \\ m_{H^0}^2 &= \mu_2^2 + \lambda_L v^2 \end{aligned}$$

$$\begin{aligned}
m_{A^0}^2 &= \mu_2^2 + \lambda_S v^2 \\
m_{H^\pm}^2 &= \mu_2^2 + \frac{1}{2} \lambda_3 v^2
\end{aligned}
\tag{3}$$

where $\lambda_{L,S}$ are defined as

$$\lambda_{L,S} = \frac{1}{2}(\lambda_3 + \lambda_4 \pm \lambda_5)
\tag{4}$$

From above relations, one can easily find the expressions of λ_i as a function of physical masses:

$$\begin{aligned}
\lambda_1 &= \frac{m_{h^0}^2}{2v^2} \\
\lambda_3 &= \frac{2(m_{H^\pm}^2 - \mu_2^2)}{v^2} \\
\lambda_4 &= \frac{(m_{H^0}^2 + m_{A^0}^2 - 2m_{H^\pm}^2)}{v^2} \\
\lambda_5 &= \frac{(m_{H^0}^2 - m_{A^0}^2)}{v^2}
\end{aligned}
\tag{5}$$

The IDM involves eight independent parameters: five $\lambda_{1,\dots,5}$, μ_1 , μ_2 and the VEV. One parameter can be eliminated by using the minimization condition, while the VEV is fixed by the Z boson mass, fine-structure constant and Fermi constant G_F . Finally, we are left with six independent parameters, which we choose as follows

$$\{\mu_2^2, \lambda_2, m_{h^0}, m_{H^\pm}, m_{H^0}, m_{A^0}\}
\tag{6}$$

One alternative parametrization is to use λ_L or λ_S in place of μ_2^2 , as can be seen from Eq. (3). The advantage of such parametrization is that it is directly connected to the evaluation of the relic density.

For completeness, we list below the triple and quartic scalar couplings that are needed in our numerical analysis:

$$\begin{aligned}
h^0 H^\pm H^\mp &= -v\lambda_3 \equiv v\lambda_{h^0 H^\pm H^\mp} \equiv v\lambda_{h^0 SS} \\
H^\pm H^\mp H^\pm H^\mp &= -4\lambda_2 \\
G^\pm H^\mp H^0 &= \frac{v}{2}(\lambda_4 + \lambda_5) \\
G^\pm H^\mp A^0 &= \pm \frac{v}{2}(-\lambda_4 + \lambda_5)
\end{aligned}
\tag{7}$$

It is clear that the triple coupling $h^0 H^\pm H^\mp$ is proportional to λ_3 which in turn is proportional to $(m_{H^\pm}^2 - \mu_2^2)$ as given in Eq. (5).

2.2 The IDM parameter space and constraints

In this work, we study in the same parameter space as in our previous work [85]. The parameter space is obtained by scanning the whole space with certain theoretical and experimental constraints. The constraints used are summarized as follows:

2.2.1 Theoretical constraints

The parameters of the IDM are subject to several theoretical constraints that we shall impose throughout our numerical analysis.

- Perturbativity:

We require that each of the quartic couplings of the scalar potential in Eq. (2) is perturbative:

$$|\lambda_i| \leq 8\pi. \quad (8)$$

- Vacuum stability:

In order to ensure vacuum stability, the potential V should remain positive when the values of scalar fields become extremely large [32]. From this condition, we have the following set of constraints on the IDM parameters (for a review, see [31]):

$$\lambda_{1,2} > 0 \quad \text{and} \quad \lambda_3 + \lambda_4 - |\lambda_5| + 2\sqrt{\lambda_1\lambda_2} > 0 \quad \text{and} \quad \lambda_3 + 2\sqrt{\lambda_1\lambda_2} > 0. \quad (9)$$

- Charge-breaking minima:

A neutral charge-conserving vacuum can be guaranteed by demanding that [111]

$$\lambda_4 - |\lambda_5| \leq 0. \quad (10)$$

- Inert vacuum:

We impose the following conditions in order to insure that the inert vacuum is the global one [111]:

$$m_{h^0}^2, m_{H^0}^2, m_{A^0}^2, m_{H^\pm}^2 > 0 \quad \text{and} \quad v^2 > -\mu_2^2/\sqrt{\lambda_1\lambda_2}. \quad (11)$$

- Unitarity:

As in the SM, the couplings of the IDM have to satisfy certain relations in order to obey unitarity. The tree-level perturbative unitarity is imposed on the various scattering amplitudes of scalar bosons at high energy. From the technique developed in [112], we find the following set of eigenvalues:

$$e_{1,2} = \lambda_3 \pm \lambda_4 \quad , \quad e_{3,4} = \lambda_3 \pm \lambda_5 \quad (12)$$

$$e_{5,6} = \lambda_3 + 2\lambda_4 \pm 3\lambda_5 \quad , \quad e_{7,8} = -\lambda_1 - \lambda_2 \pm \sqrt{(\lambda_1 - \lambda_2)^2 + \lambda_4^2} \quad (13)$$

$$e_{9,10} = -3\lambda_1 - 3\lambda_2 \pm \sqrt{9(\lambda_1 - \lambda_2)^2 + (2\lambda_3 + \lambda_4)^2} \quad (14)$$

$$e_{11,12} = -\lambda_1 - \lambda_2 \pm \sqrt{(\lambda_1 - \lambda_2)^2 + \lambda_5^2} \quad (15)$$

We impose perturbative unitarity constraint on all e_i s: $e_i \leq 8\pi$, $\forall i = 1, \dots, 12$.

It is important to note that we did not take into account higher-order corrections to the bounded from below, global minimum, and perturbative unitarity constraints. We have only included the constraints at lowest order. However, the parameter space will change if we use those constraints at NLO. For example, it has been shown in [113] that the bounded from below conditions at one-loop level can change the stability of the electroweak vacuum, and the allowed parameter space for coexisting inert and inertlike minima at NLO is larger compared to the one observed at LO. Furthermore, for the unitarity constraints beyond the lowest order that have been analyzed in the 2HDM [114], it was found that perturbative NLO unitarity constraints are stronger than the LO ones. Therefore, the allowed ranges of the quartic λ_i couplings, the inert scalar masses, and their mass differences will change if we use the NLO unitarity conditions.

2.2.2 Experimental constraints

The parameter space of the scalar potential of the IDM should also satisfy experimental search constraints. We will consider the following experimental constraints (for further details about these constraints see our previous published work [85]):

- Higgs data at the LHC [115, 116].
- The bound on the invisible Higgs decay [117].
- The direct collider searches from the LEP [44, 62, 108, 118]
- The indirect searches from electroweak precision tests [41, 119, 120].
- The data from dark matter searches [61, 64, 121–131].

3 Radiative corrections to $e^+e^- \rightarrow H^+H^-$

3.1 $e^+e^- \rightarrow H^+H^-$ at tree level

Due to the extremely small value of the electron mass and the corresponding Yukawa couplings, it is numerically justified to neglect the contributions proportional to the mass of electron, such as Feynman diagrams involving $e^+e^-h^0$, $e^+e^-G^0$, $e^-\bar{\nu}_e G^+$, and $e^+\nu_e G^-$ vertices. For this reason, the Feynman diagrams contributing to $e^+e^- \rightarrow H^+H^-$ at the tree level are mediated by the γ and Z s-channel exchange as shown in Figure 3.1.

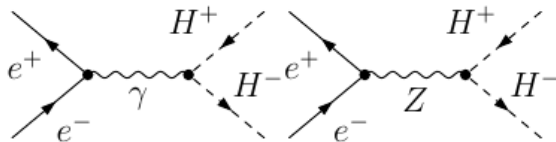


Figure 3.1: Tree level Feynman diagrams for $e^+e^- \rightarrow H^+H^-$ are shown.

Using the covariant derivative of the Higgs doublet, one can derive the scalar coupling to gauge bosons. We list below a part of the Lagrangian needed for our study

$$\begin{aligned} \mathcal{L}_{VH^+H^-, VVH^+H^-} = & \left[-ieA^\mu + ie\frac{(c_W^2 - s_W^2)}{2c_W s_W} Z^\mu \right] H^+ \overleftrightarrow{\partial}_\mu H^- \\ & + \left[e^2 A^\mu A_\mu - e^2 \frac{(c_W^2 - s_W^2)}{c_W s_W} Z^\mu A_\mu \right] H^+ H^- \end{aligned} \quad (16)$$

where e is the electric charge and $c_W \equiv \cos \theta_W$ ($s_W \equiv \sin \theta_W$) with θ_W being the Weinberg mixing angle. It is clear from above equation that the interactions involving charged scalar depend only on the electric charge and the Weinberg mixing angle θ_W .

Let $p_{1,2}$ and $k_{1,2}$ be the momenta of incoming e^\pm and outgoing H^\pm , respectively, and define the Mandelstam variables as

$$\begin{aligned} s &= (p_1 + p_2)^2 = (k_1 + k_2)^2 \\ t &= (p_1 - k_1)^2 = (p_2 - k_2)^2 \\ u &= (p_1 - k_2)^2 = (p_2 - k_1)^2 \end{aligned} \quad (17)$$

The matrix elements at tree level for the two contributions have the following form:

$$\mathcal{M}_0^\gamma = -2 \frac{e^2}{s} \bar{v}(p_2) \not{k}_1 u(p_1), \quad (18)$$

$$\mathcal{M}_0^Z = 2 \frac{e^2 g_H}{s - m_Z^2} \left(g_V \bar{v}(p_2) \not{k}_1 u(p_1) - g_A \bar{v}(p_2) \not{k}_1 \gamma^5 u(p_1) \right) \quad (19)$$

with

$$g_V = \frac{1 - 4s_W^2}{4c_W s_W}, \quad g_A = \frac{1}{4c_W s_W}, \quad g_H = -\frac{c_W^2 - s_W^2}{2c_W s_W}.$$

The total matrix element is then given by

$$\mathcal{M}_0 = \mathcal{M}_0^\gamma + \mathcal{M}_0^Z \quad (20)$$

and the total cross section can be written as

$$\sigma^0 = \frac{\pi \alpha^2 \beta^3}{3s} \left[1 + g_H^2 \frac{g_V^2 + g_A^2}{(1 - m_Z^2/s)^2} - \frac{2g_H g_V}{1 - m_Z^2/s} \right], \quad (21)$$

where $\beta = \sqrt{1 - 4m_{H^\pm}^2/s}$ is the velocity of outgoing H^\pm in the c.m. frame. Note that the first term comes from the photon exchange, the second term comes from the Z boson exchange while the third one is the interference between the photon and Z boson exchange.

This cross section is only related to the mass of H^\pm and it is independent of the other four parameters $\mu_2^2, \lambda_2, m_{H^0}, m_{A^0}$. It should be reminded that, near the threshold regions, it drops quickly due to the phase space suppression factor β^3 .

Lastly, as the collision energy is assumed to be 250 GeV or even higher, the intermediate Z boson is always far away from its mass shell. Hence, we have neglected the effects of decay width of Z boson in this work.

3.2 $e^+e^- \rightarrow H^+H^-$ at one loop

The 't Hooft-Feynman gauge has been used to evaluate both the weak corrections as well as the QED ones. The generic Feynman diagrams for $e^+e^- \rightarrow H^+H^-$ are drawn in Fig. 3.2, which can be put into six categories:

1. One-loop corrections to the initial state vertices e^+e^-V ($V = \gamma, Z$) which are purely SM, G_1 and G_2 .
2. One-loop corrections to the vertices VH^+H^- ($V = \gamma, Z$), G_3 to G_{11} .
3. One-loop corrections to photon and Z boson propagators as well as γ - Z , G_{12} to G_{18} . Note that the mixing Z - G^0 and γ - G^0 in the s -channel contribution was not included. Due to Lorentz invariance, such mixing would be proportional to $(p_1 + p_2)^\mu$, which after contracting with the initial state e^+e^- will be proportional to m_e and thereafter will vanish.
4. Box contributions, G_{19} to G_{21} .
5. The various counterterms for initial and final states and also the γ and Z propagators, γ - Z mixings are also depicted in G_{22} to G_{24} .

Moreover, we also add real photon emission $e^+e^- \rightarrow H^+H^-\gamma$ which is depicted in diagrams G_{25} to G_{29} . Note that diagram G_{27} does not contain IR divergence but it is an important piece for electromagnetic gauge invariance.

Let M_V be the matrix element of all these diagrams, the virtual corrections at NLO can be expressed as

$$d\sigma_V \propto 2\text{Re}\bar{\Sigma} \left(M_0 M_V^\dagger \right).$$

Since we have omitted the decay width of the intermediate Z boson in the leading order matrix element M_0 , at fixed order we can only take into account the real part of M_V . This also means that we can neglect the imaginary parts of diagrams G_{12} to G_{18} , which contribute to the decay width of the Z boson at higher orders when both vector bosons V attached to the loop are Z bosons.

Calculation of the one-loop corrections will lead to ultraviolet (UV) as well as IR divergences. The UV singularities are treated in the on-shell renormalization scheme after being regularized using dimensional regularization while the IR divergences arising from the diagrams involving a photon are regularized with a small fictitious photon mass λ and have to cancel with the ones from real photon emissions.

The unbroken \mathbb{Z}_2 symmetry prevents the mixing between the SM doublet H_1 and the inert doublet H_2 which significantly facilitates the renormalization of the IDM. The full renormalization of this model has been presented in [90]. In our work, we will use the on-shell scheme developed first for the SM in [132–134], completed by the on-shell renormalization scheme for the inert scalar fields and their masses.

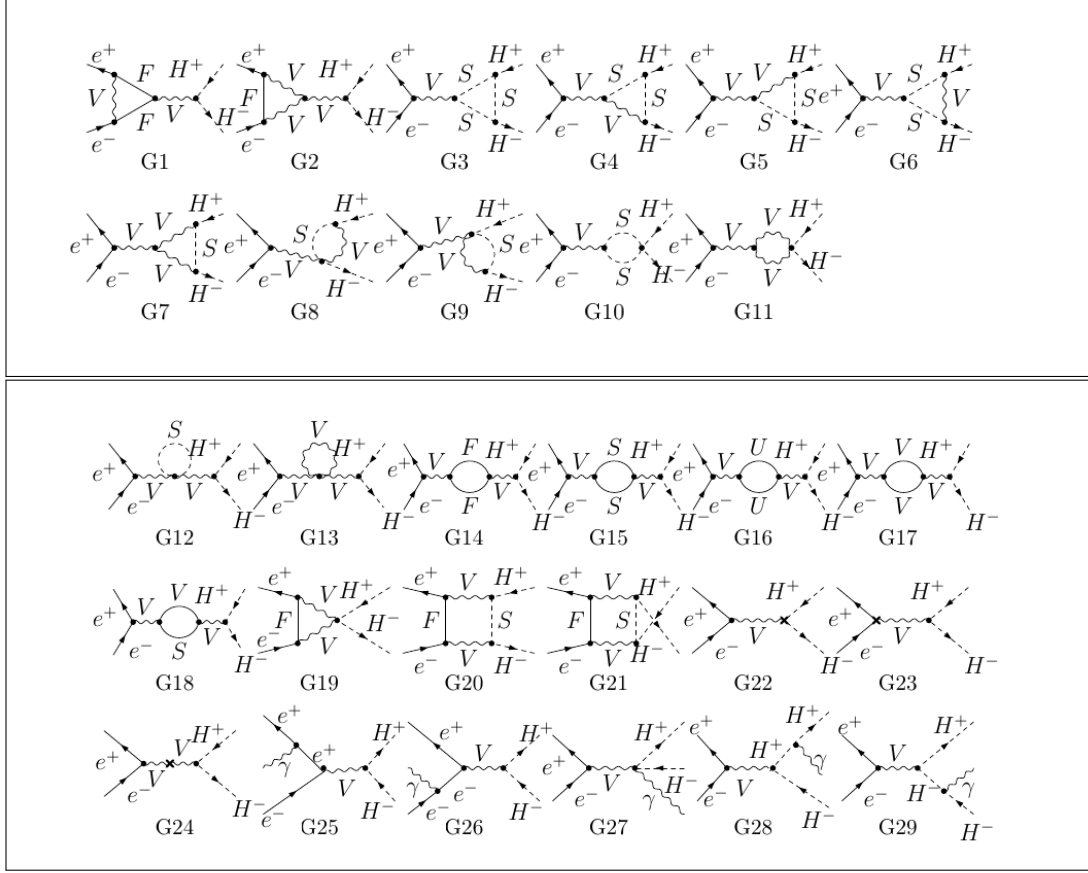


Figure 3.2: Generic one-loop Feynman diagrams for $e^+e^- \rightarrow H^+H^-$ are shown, where F stands for SM fermions; V stands for generic vector bosons which could be γ , Z , or W^\pm ; and S could be either a Goldstone G^0 , G^\pm or a Higgs boson h^0 , H^0 , A^0 , or H^\pm .

Concerning the renormalization of the SM parameters and fields, we refer to [134, 135]. For the renormalization of charge, an $\alpha(m_Z)$ scheme is used, following the procedure in Refs. [134, 135]. The charge is first renormalized in the Thomson limit and then switched effectively to m_Z by resumming large logarithms from light fermions, which gives

$$\alpha(m_Z) = \frac{\alpha(0)}{1 - (\Delta\alpha(m_Z))_{f \neq \text{top}}}, \quad (22)$$

with

$$(\Delta\alpha(m_Z))_{f \neq \text{top}} = \Pi_{f \neq \text{top}}(0) - \text{Re}\Pi_{f \neq \text{top}}(m_Z^2) \quad (23)$$

and $\alpha(0)$ is the coupling constant renormalized in the Thomson limit. More details about this renormalization scheme can be found in Appendix A, where the uncertainties from different schemes are also discussed. Following the notation in PDG [120], Eq. (22) is regarded as an “on shell” definition of the running coupling constant at the scale m_Z .

For the renormalization of the inert scalar bosons, we use a similar approach as in [134, 135]. Because of the exact \mathbb{Z}_2 symmetry, there is no mixing between H^\pm - W^\mp and H^\pm - G^\mp , this makes the renormalization of the scalar fields easier. The Higgs wave function renormalization constant and mass counterterm are fixed by the two following on-shell conditions :

- The on-shell condition for the physical mass m_{H^\pm} .
- The propagator of the charged scalar must have residue 1 at the pole mass.

These requirements will lead, respectively, to

$$\begin{aligned} \text{Re}\hat{\Sigma}_{H^\pm H^\pm}(m_{H^\pm}^2) &= 0 \\ \text{Re}\frac{\partial\hat{\Sigma}_{H^\pm H^\pm}(k^2)}{\partial k^2}\Bigg|_{k^2=m_{H^\pm}^2} &= 0, \end{aligned} \quad (24)$$

where $\hat{\Sigma}_{H^\pm H^\pm}$ is the one-loop renormalized charged scalar self-energy, i.e.

$$\hat{\Sigma}_{H^\pm H^\pm}(k^2) = \Sigma_{H^\pm H^\pm}(k^2) - \delta m_{H^\pm}^2 + (k^2 - m_{H^\pm}^2)\delta Z_{H^\pm}. \quad (25)$$

Here $\Sigma_{H^\pm H^\pm}$ is the one-loop unrenormalized charged scalar self energy.

All the SM renormalization constants defined above can be found in [134, 135]. Using the condition in Eq. (24) and the relation in Eq. (25), one can prove that

$$\delta Z_{H^\pm} = -\text{Re}\frac{\partial\Sigma_{H^\pm H^\pm}(k^2)}{\partial k^2}\Bigg|_{k^2=m_{H^\pm}^2}. \quad (26)$$

The explicit expression for δZ_{H^\pm} is presented in Appendix B.

For the counterterms, only two are new here comparing with the SM. They are listed as follows:

$$\begin{aligned} \delta\mathcal{L}_{AH^+H^-} &= -ie(\delta Z_e + \delta Z_{H^\pm} + \frac{\delta Z_{AA}}{2} + g_H \frac{\delta Z_{AZ}}{2})A^\mu H^+ \overleftrightarrow{\partial}_\mu H^- \\ \delta\mathcal{L}_{ZH^+H^-} &= -ieg_H(\delta Z_e + \delta Z_{H^\pm} + \frac{\delta Z_{ZZ}}{2} - \frac{\delta s_W}{(c_W^2 - s_W^2)c_W^2 s_W} + \frac{\delta Z_{AZ}}{2g_H})Z^\mu H^+ \overleftrightarrow{\partial}_\mu H^- \end{aligned} \quad (27)$$

For the counterterms of the initial state vertices: $e^+e^-\gamma$ and e^+e^-Z , counterterm of the Z boson, the photon propagators, and their mixing, they are exactly the same as in the SM and can be found in [134, 135].

With such a “completely on-shell” renormalization scheme, our results are totally independent of the renormalization scale μ_r . As an alternative, they now depend on the new scale introduced during the renormalization of charge (set to m_Z in this work).

As mentioned before, Feynman gauge is used in our calculation. Strictly speaking, to ensure our results are gauge invariant, calculation with another gauge is needed. However this will lead to a totally different model file and/or modifications in the automatic package, which is beyond our abilities at present. Hence, we can only believe that this is automatically ensured by the theory, and only check those within our abilities (such as current conservation in real emissions).

On the other hand, as already known in the renormalization of 2HDM, improper treatment of tadpole contributions may lead to gauge-dependent results (see e.g. [136–138]). Fortunately, compared with the general 2HDM, the IDM is simple on this issue since there is no mixing between the two doublets. Hence, we can apply the same treatment as in the SM and avoid such an issue.

Let us now discuss the treatment of the IR divergences, which includes two parts, one is from virtual corrections, the other is from real emission. As mentioned before, IR divergences in

this work are regularized by introducing a small fictitious photon mass, λ . The IR divergences in virtual corrections are present in four sources: (i) wave function renormalization of charged particles such as electrons and charged scalars; (ii) vertex corrections to $e^+e^-\gamma$ and e^+e^-Z , G_1 in Fig. 3.2 with $V = \gamma$, where incoming electron and positron exchange a virtual photon with each other; (iii) in the case of $e^+e^- \rightarrow H^+H^-$ vertex corrections to γH^+H^- and ZH^+H^- : G_6 in Fig. 3.2 with $V = \gamma$ where the outgoing charged scalar pair exchanges a virtual photon ; (iv) in case of $e^+e^- \rightarrow H^+H^-$ box corrections: G_{20} and G_{21} in Fig. 3.2 with $(V, V) = (\gamma, \gamma)$ or $(V, V) = (\gamma, Z)$ where incoming fermions exchange one or two virtual photons with outgoing charged scalars.

IR divergence in real emission comes from phase space integration. Besides λ , two cutoffs ΔE and $\Delta\theta$ are introduced to deal with the IR singularities in real photon emission based on the two cutoff phase space slicing method [139]. $\Delta E = \delta_s \sqrt{s}/2$ defines the soft photon energy cutoff for the bremsstrahlung process. It can be viewed as the photon energy cut that separates the soft and hard regions. The angle $\Delta\theta$ further separates the hard part into hard-collinear and hard-noncollinear regions. The NLO corrections are then decomposed into the virtual, soft, hard-collinear, and hard noncollinear parts as follows:

$$d\sigma^1 = d\sigma_V(\lambda) + d\sigma_S(\lambda, \Delta E) + d\sigma_{HC+CT}(\Delta E, \Delta\theta) + d\sigma_{H\bar{C}}(\Delta E, \Delta\theta) \quad (28)$$

Here S , HC , and $H\bar{C}$ denote the contributions of soft, hard-collinear, and hard-noncollinear parts from real photon emission, respectively. V denotes the virtual corrections including loop and counterterm diagrams. CT in the third term of rhs denotes the extra contribution arising from the structure function of incoming electron and positron. More details about the treatment of IR divergence are presented in Appendix C, as well as the checks of our results for the independence of cutoffs.

The total cross section at NLO σ^{NLO} , is the sum of LO cross section σ^0 and NLO corrections σ^1 , namely

$$\sigma^{\text{NLO}} = \sigma^0 + \sigma^1 \equiv \sigma^0(1 + \Delta), \quad (29)$$

where Δ is the relative correction.

As described in Sec. 3.1 of Ref. [140], the NLO electroweak corrections can be safely grouped into two gauge-invariant parts:

1. The “QED” part, which includes all the diagrams that contain an extra photon attached to the LO diagrams. These diagrams can be easily found by investigating the generic Feynman diagrams in Fig. 3.2 and we list them here:
 - G_1 when the vector boson connected with the incoming electron pair is a photon;
 - G_6 when the vector boson connected with the outgoing charged scalar pair is a photon;
 - G_8 and G_9 when the vector boson connected with the outgoing charged scalar pair is a photon;
 - G_{19} , G_{20} , and G_{21} when either vector boson is a photon;
 - G_{25} to G_{29} : all real emission diagrams.

Meanwhile, the photonics contribution to the wave function renormalization of the electron and charged scalar is also grouped into this part.

2. The “weak” part, which contains all the remaining contributions.

It should be noted that the “QED” part here is only a gauge-invariant subgroup of the whole QED corrections. There are remaining QED corrections in the “weak” part. Actually, it is very hard, if not impossible in this process, to separate the whole QED part because of $\gamma - Z$ mixing.

The relative correction is then separated into two parts correspondingly, i.e. we have

$$\Delta = \Delta_{\text{weak}} + \Delta_{\text{QED}}. \quad (30)$$

Similar to the pair production of W bosons or top quarks, the Coulomb singularity appears in one-loop corrections, which is proportional to $\alpha\pi/\beta$ [141, 142]. It gives an important enhancement to the cross section near the threshold. This effect is already well known and can be resummed to all orders. After the resummation, the LO cross section becomes

$$\sigma^0 \rightarrow \sigma_{\text{resum.}}^0 = |\psi(0)|^2 \sigma^0, \quad (31)$$

where we have used the “resum.” as the abbreviation of resummed in the subscript to label the quantities after the resummation. The factor $|\psi(0)|^2$, which was originally obtained by Sommerfeld [143] and Sakharov [144], is given by

$$|\psi(0)|^2 = \frac{X}{1 - e^{-X}} = 1 + \frac{X}{2} + \frac{X^2}{12} + \dots \quad (32)$$

where $X = \alpha\pi/\beta$.

Beyond LO, we assume that the resummed cross section can still be written into the product of two parts, similar to Eq. (31). The first part is a factor that resums all the Coulomb singularities. Here we use $|\psi(0)|^2$ as this factor since we only resum the leading Coulomb singularities. The second component represents a hard part which contains no more Coulomb singularities and can be calculated order by order perturbatively. Namely, we suppose

$$\sigma_{\text{resum.}} = |\psi(0)|^2 \sigma_{\text{H}}. \quad (33)$$

Here the label “H” denotes the hard part. Expanding the rhs of Eq. (33) to LO in α and then matching it with LO cross section σ^0 , it gives

$$\sigma_{\text{H}}^0 = \sigma^0. \quad (34)$$

This means that the LO resummed cross section in Eq. (31) is correctly reproduced. Now expanding the rhs of Eq. (33) again to NLO in α and matching it with NLO cross section σ^{NLO} , it gives

$$\sigma_{\text{H}}^0 + \frac{X}{2} \sigma_{\text{H}}^0 + \sigma_{\text{H}}^1 = \sigma^{\text{NLO}}. \quad (35)$$

Inserting Eqs. (29) and (34) into Eq. (35) and solving σ_{H}^1 from it, it gives

$$\sigma_{\text{H}}^1 = \sigma^0 \left(\Delta - \frac{X}{2} \right) \equiv \sigma^0 \Delta_{\text{H}}. \quad (36)$$

Here, Δ_{H} represents the ratio of σ_{H}^1 to σ_{H}^0 . In our work, numerical analysis has confirmed that Δ_{H} does not exhibit any further Coulomb singularities. This implies that Eq. (33) works at least up to one-loop order. Then, the resummed cross section at NLO is derived as follows:

$$\sigma_{\text{resum.}}^{\text{NLO}} = |\psi(0)|^2 (\sigma_{\text{H}}^0 + \sigma_{\text{H}}^1) = |\psi(0)|^2 \sigma^0 (1 + \Delta_{\text{H}}). \quad (37)$$

Expanding $\sigma_{\text{resum.}}^{\text{NLO}}$ to even higher in α , it gives

$$\sigma_{\text{resum.}}^{\text{NLO}} = \sigma_{\text{H}}^0 + \left(\sigma_{\text{H}}^0 \frac{X}{2} + \sigma_{\text{H}}^1 \right) + \left(\sigma_{\text{H}}^0 \frac{X^2}{12} + \sigma_{\text{H}}^1 \frac{X}{2} \right) + \mathcal{O}(\alpha^5). \quad (38)$$

The first three terms on the rhs are the contributions of $\mathcal{O}(\alpha^2)$, $\mathcal{O}(\alpha^3)$, and $\mathcal{O}(\alpha^4)$, respectively. The third term stands for two different cases of Coulomb singularity at next-to-next-to-leading order. $\sigma_{\text{H}}^0 X^2/12$ corresponds to the exchange of two soft photons in the final states, while $\sigma_{\text{H}}^1 X/2$ corresponds to the exchange of one soft photon in the final states. On the other hand, Δ_{H} can also be separated into its QED and weak parts, similar to what is done for Δ in Eq. (30). This separation is expressed as

$$\Delta_{\text{H}} = \Delta_{\text{H,QED}} + \Delta_{\text{H,weak}}. \quad (39)$$

Due to the fact that Coulomb singularity is caused by soft photon exchange in the final states, it should belong to the QED part, namely we have

$$\Delta_{\text{H,QED}} = \Delta_{\text{QED}} - \frac{X}{2}, \quad \Delta_{\text{H,weak}} = \Delta_{\text{weak}}. \quad (40)$$

It has also been confirmed numerically that $\Delta_{\text{H,QED}}$ remains finite when the velocity of outgoing charged pair goes to zero.

Up to this point, we have effectively addressed the treatment of Coulomb singularities and obtained resummed cross sections. However, in this work, we are more interested in relative corrections, not only the cross sections. Let $\Delta_{\text{resum.}}$ be the ratio of relative corrections after resummation ($\sigma_{\text{resum.}}^{\text{NLO}}/\sigma_{\text{resum.}}^0 - 1$). Due to the fact that $|\psi(0)|^2$ acts as a global factor in both LO and NLO cross sections, $\Delta_{\text{resum.}}$ is always equal to the ratio of hard part, Δ_{H} . Correspondingly, we also have

$$\Delta_{\text{resum.,QED}} = \Delta_{\text{H,QED}} = \Delta_{\text{QED}} - \frac{X}{2}, \quad \Delta_{\text{resum.,weak}} = \Delta_{\text{H,weak}} = \Delta_{\text{weak}}. \quad (41)$$

In order to show the effect of this resummation technique, we present in a certain case the cross section and relative corrections before and after the resummation in Table 3.1. There are a few comments on the results in the table:

- The relative weak corrections remain constant both before and after resummation, meaning that $\Delta_{\text{resum.,weak}}$ maintains its equality to Δ_{weak} throughout.
- The resummation mostly affects the results near the threshold, i.e. the region where β is small and close to 0. When β is varying from 0.9165 to 0.0283, it is observed that the QED corrections can change from 1.628% to 42.143%.
- Before the resummation, the LO cross section can be changed drastically by the QED corrections, especially near the threshold region. After the resummation, the QED corrections are small and well controlled within a size around 1%. The LO cross section is enhanced directly by the factor $|\psi(0)|^2$ during the resummation, which varies from 1.0134 to 1.4918 as β decreases. While the NLO cross section is much more stable in this process. From the data before and after the resummation we can see the ratio is always around 1 (from 0.999 to 1.039 as β decreases).

m_{H^\pm} (GeV)	100	150	200	225	245	249	249.9
β	0.9165	0.8000	0.6000	0.4359	0.1990	0.0894	0.0283
$ \psi(0) ^2$	1.0134	1.0153	1.0204	1.0282	1.0625	1.1425	1.4918
Before Resummation							
σ^0 (fb)	95.320	63.392	26.744	10.254	0.976	0.0883	0.00280
σ^{NLO} (fb)	90.344	60.288	25.783	10.085	1.004	0.0970	0.00389
$\Delta_{\text{QED}}(\%)$	1.628	1.711	2.101	2.731	5.738	12.911	42.143
$\Delta_{\text{weak}}(\%)$	-6.859	-6.609	-5.695	-4.379	-2.869	-3.058	-3.175
After Resummation							
$\sigma_{\text{resum.}}^0$ (fb)	96.593	64.362	27.291	10.543	1.037	0.1009	0.00418
$\sigma_{\text{resum.}}^{\text{NLO}}$ (fb)	90.256	60.230	25.756	10.075	1.003	0.0971	0.00401
$\Delta_{\text{resum.,QED}}(\%)$	0.299	0.189	0.071	-0.064	-0.384	-0.723	-0.933
$\Delta_{\text{resum.,weak}}(\%)$	-6.859	-6.609	-5.695	-4.379	-2.869	-3.058	-3.175

Table 3.1: Cross section and relative corrections before (second block) and after (third block) the resummation of the Coulomb singularity with $\sqrt{s} = 500$ GeV are demonstrated. The remaining IDM parameters are chosen as $m_{H^0} = m_{A^0} = m_{H^\pm}$, $\lambda_2 = 2$, and $\mu_2^2 = 0$. Quantities before resummation, σ^0 , σ^{NLO} , Δ_{QED} , and Δ_{weak} , are obtained with Eqs. (21), (29), and (30). Quantities after resummation, $\sigma_{\text{resum.}}^0$, $\sigma_{\text{resum.}}^{\text{NLO}}$, $\Delta_{\text{resum.,QED}}$, and $\Delta_{\text{resum.,weak}}$, are obtained with Eqs. (31), (36), (37), and (41).

- Throughout the entire region, the QED corrections decrease by at least one order of magnitude after resummation. This observation strongly suggests that the dominant factor contributing to the QED corrections is the Coulomb singularity term.

All of this demonstrates that the resummation is necessary and effective. In the following discussion, we will use σ or Δ to refer to the resummed values, and for convenience, we will omit the subscript “resum.”

4 Numerical results

In the present work, the computation of all the one-loop matrix elements and counter-terms is performed with the help of **FeynArts** and **FormCalc** [145–147] packages. The scalar integrals are numerically evaluated using **LoopTools** [148,149]. The other parts are obtained with the help of **FDC** [150] and **BASES** [151]. The cancellation of UV divergences are obtained both analytically and numerically. It should be noted that the model file of IDM, including all needed renormalization counter terms and renormalization constants, is obtained by manually modifying the SM model file. We have checked this model file with the output from **FeynRules** and confirmed their agreement. Recently, an automatic tool **NLOCT** [152], which can automatically generate counter terms and calculate renormalization constants, became available. It provides a model for 2HDM that can be used in one-loop QCD and EW calculation. However, compared with the general 2HDM, IDM is simple because there is no mixing between the two doublets. Hence, we use our own model file mentioned above.

In this section, we present our numerical results for our process $e^+e^- \rightarrow H^+H^-$. It has been pointed out that the triple Higgs couplings can cause a large (can go up to 30%) radiative correction to the process $e^+e^- \rightarrow H^+H^-$ [102,105] in the 2HDM. Below we examine the radiative corrections to our process in the IDM and we expect that the electroweak radiative corrections to $e^+e^- \rightarrow H^+H^-$ would have some similarities with $e^+e^- \rightarrow H^0A^0$ [85]. For the QED corrections,

we will study both soft photon emission as well as the hard one.

4.1 Numerical input

We adopt the following numerical values of the physical parameters from PDG [120]:

1. The fine structure constant: $\alpha(0) = 1/137.036$, $\alpha(m_Z) = 1/128.943$ with $\Delta\alpha_{\text{hadron}}^{(5)}(m_Z) = 0.02764$.
2. The gauge boson masses: $m_W = 80.379$ GeV and $m_Z = 91.188$ GeV.
3. The fermion masses:

$$\begin{aligned} m_e &= 0.511 \text{ MeV} & m_u &= 0.134 \text{ GeV} & m_t &= 173.2 \text{ GeV}, \\ m_\mu &= 0.106 \text{ GeV} & m_d &= 0.134 \text{ GeV} & m_b &= 4.660 \text{ GeV}, \\ m_\tau &= 1.777 \text{ GeV} & m_s &= 0.095 \text{ GeV} & m_c &= 1.275 \text{ GeV}. \end{aligned}$$

The masses of u and d are taken as effective parameters to reproduce $\Delta\alpha_{\text{hadron}}^{(5)}(m_Z)$ with $\alpha(m_Z)$. They are obtained as $m_u = m_d = 0.134$ GeV.

In the IDM, the CP even Higgs boson h^0 is the only SM-like Higgs boson observed by the LHC collaborations, and we use $m_{h^0} = 125.18$ GeV. For the other IDM parameters, we perform a scan over the whole parameter space, which includes the physical masses m_{A^0} , m_{H^0} and m_{H^\pm} , μ_2^2 and λ_2 parameters. We take into account all the experimental constraints as well as the theoretical requirements given in the Sec. 2.2.

It is found that our numerical results are almost independent of the λ_2 parameter. Consequently, we will fix $\lambda_2 = 2$ in the next part.

In the following, we will use the $\alpha(m_Z)$ scheme described before to present our results.

4.2 Weak corrections in three scenarios

In our numerical analysis, we will consider three scenarios, which are tabulated in Table 4.1. They are categorized in terms of degenerate/nondegenerate between inert scalar boson masses, with/without invisible Higgs decay, and with/without DM constraints. It is thought that scenario I is the simplest one with only three free parameters and is the easiest one to demonstrate the one-loop corrections, while scenario III might be more realistic after taking into account collider experimental bounds and dark matter constraints and six benchmark points are chosen from this scenario for the LHC and future collider searches.

Our numerical analysis begins with scenario I, which has only three free parameters to consider. When λ_2 is fixed, there are only two free parameters (μ_2^2 and $m_S = m_{H^0} = m_{A^0} = m_{H^\pm}$) to vary. Three typical collision energies of future e^+e^- colliders, namely: $\sqrt{s} = 250$ GeV, $\sqrt{s} = 500$ GeV and $\sqrt{s} = 1000$ GeV are chosen to expose the effects of new physics.

It should be mentioned that when the charged scalar mass is fixed, the $h^0 H^+ H^-$ coupling is simply determined by the parameter μ_2^2 , as given in Eq. (5). Therefore, in order to examine how the theoretical parameters like μ_2^2 and m_{H^\pm} can affect the cross section and how theoretical constraints and experimental bounds can affect allowed parameter space, we introduce five cases with different values of μ_2^2 given in Table 4.2. These values of μ_2^2 corresponding to five cases are chosen in the allowed parameter space which have passed all theoretical and experimental bounds and constraints, and we have labeled these results by the labels IDM1-5 in Fig. 4.1. We have deliberately introduced two with positive values and two with negative values of μ_2^2 .

	Scenario I	Scenario II	Scenario III
Theoretical constraints	✓	✓	✓
Degenerate spectrum	✓		
Higgs data	✓	✓	✓
Higgs invisible decay open		✓	✓
Direct searches from LEP	✓	✓	✓
Electroweak precision tests	✓	✓	✓
Dark matter constraints			✓

Table 4.1: Scenarios and their conditions are tabulated. Scenario I where all the inert scalars are degenerate is described by three parameters which are $(m_S = m_{H^0} = m_{A^0} = m_{H^\pm}, \mu_2^2, \lambda_2)$, scenarios II and III with a nondegenerate spectrum for the inert scalars are described by five parameters, which are $(m_{H^\pm}, m_{H^0}, m_{A^0}, \mu_2^2, \lambda_2)$.

	IDM1	IDM2	IDM3	IDM4	IDM5
$\mu_2^2(\text{GeV}^2)$	40000	6000	0	-10000	-30000

Table 4.2: In scenario I, five cases with typical values of μ_2^2 labeled as IDM1-5 are given.

In Fig. 4.1, total cross section and relative corrections to $e^+e^- \rightarrow H^+H^-$ as a function of the inert scalar masses m_S are shown in scenario I. It is observed that the allowed ranges of m_S are different when μ_2^2 takes different values. More explicitly, it is found that in the range of 100–500 GeV, the lower bounds of m_S in the cases of IDM1, IDM4 and IDM5 are constrained by the signal strength of $h^0 \rightarrow \gamma\gamma$ at the LHC, whereas the upper bound of m_S in the case of IDM5 is constrained by the unitarity condition. For example, in the IDM5 case, m_S shall not be smaller than 340 GeV, which explains why there is no IDM5 in the plot with $\sqrt{s} = 500$ GeV and there are no IDM4 and IDM5 in the plot with $\sqrt{s} = 250$ GeV.

Obviously, since the process $e^+e^- \rightarrow H^+H^-$ is s -channel dominant, when the mass of charged scalar is fixed, the cross section becomes smaller and smaller when the c.m. energy increases from 250 GeV to 1 TeV. For a fixed c.m. energy, the cross section drops quickly when the mass of charged scalar increases to the kinematic end points. It is noteworthy that a pair of light charged scalar (say 100 GeV or so) can be copiously produced and the total cross sections could be of the order of 100 fb which would lead to more than 2×10^5 events at LC machines with $\sqrt{s} = 250$ GeV which can deliver about 2 ab^{-1} luminosity.

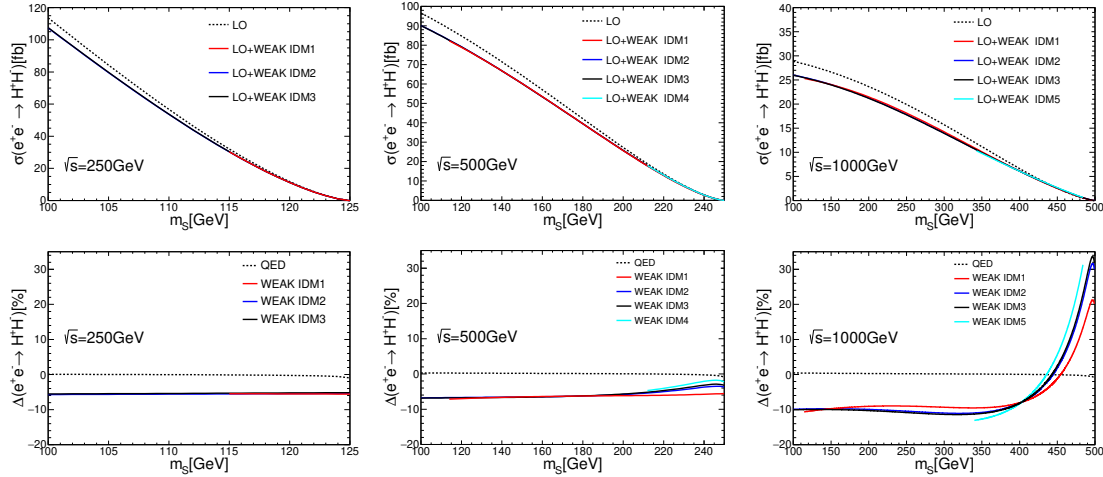


Figure 4.1: The total cross section and the ratio of EW corrections to $e^+e^- \rightarrow H^+H^-$ as a function of the inert scalar masses m_S with three collision energies $\sqrt{s} = 250$ GeV, 500 GeV, and 1000 GeV are shown in scenario I in the upper and lower panels, respectively. The corresponding values of μ_2^2 are given in Table 4.2.

It can be read from the lower panel of Fig. 4.1 that the ratio of weak corrections in the IDM can reach -6% at $\sqrt{s} = 250$ GeV, which is almost independent of the mass m_S . In contrast, at the c.m. energy $\sqrt{s} = 1$ TeV, the ratio starts from -10% and can go up to 30% or higher. Such a behavior can be attributed to the large corrections of the $h^0 H^+ H^-$ coupling. For the degenerate scenario with μ_2^2 fixed, when the parameter $m_S = m_{H^\pm}$ increases from 100 GeV to 500 GeV or so, the $h^0 H^+ H^-$ coupling proportional to λ_3 also increases almost monotonically, especially near the end point region (say $350 \text{ GeV} < m_S < 500 \text{ GeV}$). Such a $h^0 H^+ H^-$ coupling can contribute to the EW corrections both linearly via the virtual corrections to $(\gamma, Z)H^+ H^-$ vertices and quadratically via the wave function renormalization of the charged scalar. When m_S increases, the total cross sections decrease due to the suppression of phase space, while the ratio of EW corrections becomes larger and larger, as shown in the last plot of the lower panel.

With these crucial lessons on weak corrections learned from scenario I, we are ready to further explore the whole parameter spaces of the IDM and illustrate the behavior of weak corrections for all three scenarios, as shown in Fig. 4.2.

The upper panel of Fig. 4.2 is devoted to scenario I, where the ratio of EW corrections to $e^+e^- \rightarrow H^+H^-$ as a function of the inert scalar masses m_S are shown, while the $\lambda_{h^0 SS}/v = -\lambda_3$ coupling is labeled as a color bar. For the c.m. energy $\sqrt{s} = 250$ GeV, the parameter m_S can be measured in the range $[80, 125]$ GeV, and the ratio $\Delta\sigma$ can change in the range $[-5.9\%, -3.8\%]$; for the c.m. energy $\sqrt{s} = 500$ GeV, the parameter m_S is kinematically accessible up to 250 GeV and $\Delta\sigma$ can change in the range $[-7.8\%, 1\%]$. For these two cases, the ratio of EW corrections is not very significant, which is due to the fact that the range of λ_3 is limited to $[-3.5, 1.5]$. In contrast, for the c.m. energy $\sqrt{s} = 1$ TeV, the parameter m_S is kinematically accessible up to 500 GeV, which in turn implies a larger range for $\lambda_3 \in [-9, 2]$. Then the ratio of EW corrections can be in the range $[-13\%, 38\%]$. In this case, the relative corrections become substantial for m_S close to the threshold production, where the absolute values of λ_3 can be quite large (say $|\lambda_3| \sim 9$). Consequently, the relative size of loop corrections increases and can reach 40% .

For scenario II, the theoretical parameters $\lambda_{4,5}$ are nonvanishing and could contribute to the vacuum stability and unitarity constraints. Therefore, when compared with scenario I, two more dimensions are added to the theoretical parameter space. Similar to scenario I, the parameter λ_3

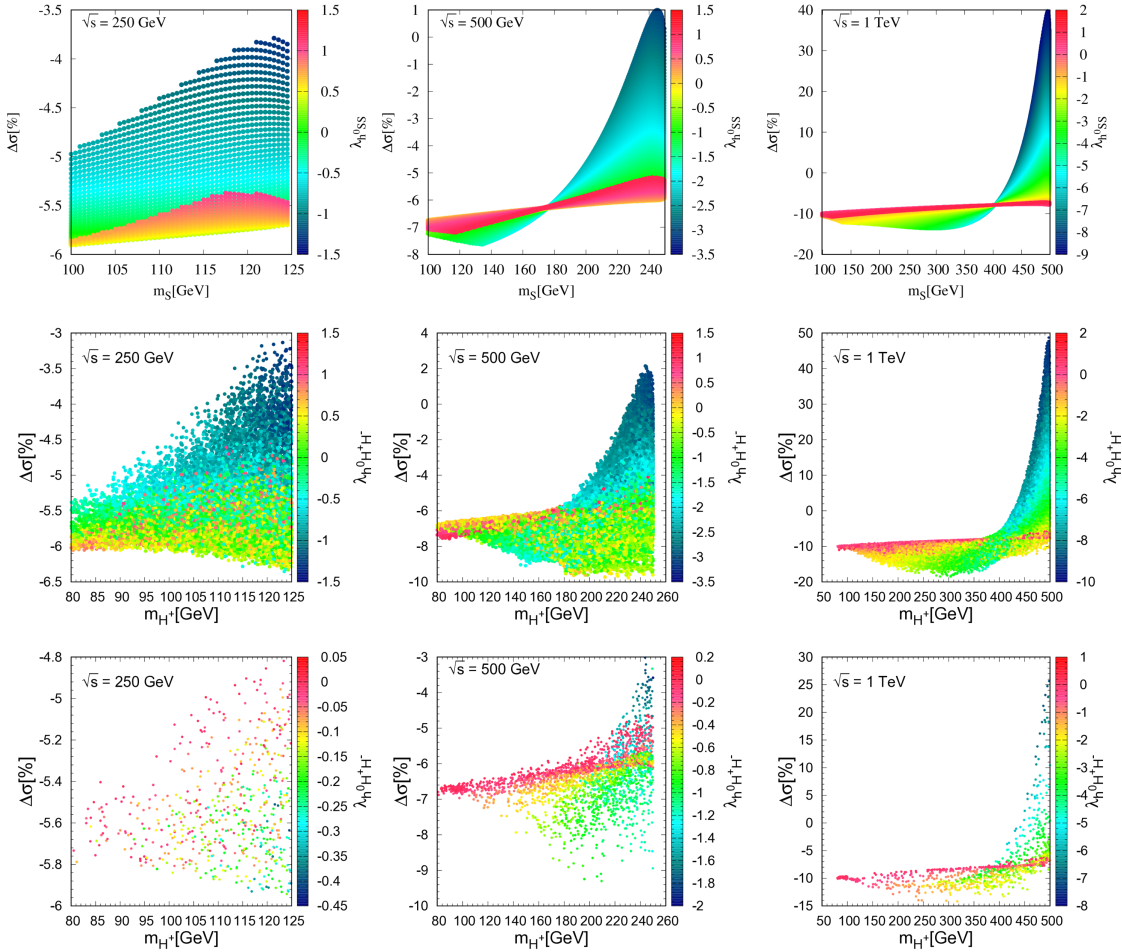


Figure 4.2: Electroweak corrections to $e^+e^- \rightarrow H^+H^-$ for $\sqrt{s} = 250$ GeV, 500 GeV, and 1000 GeV as a function of m_S and the λ_{hSS} coupling normalized to the VEV of the SM Higgs are shown. Plots in the upper panel show scenario I, and the middle and lower panels show the nondegenerate scenario before (scenario II) and after applying dark matter constraints (scenario III), respectively.

should be constrained by the Higgs data, like the branching fraction measurement of $h^0 \rightarrow \gamma\gamma$, since a light charged scalar can have a significant contribution to this branching fraction. In the case with $\sqrt{s} = 250$ GeV, as shown by the plots of the middle row of Fig. 4.2, due to kinematics, the range of charged scalar mass that the machine can measure is $[80, 125]$ GeV. It is found that the diphoton signal strength puts a severe constraint on the parameter λ_3 , which can only be within the range $[-1, 1]$. Thus, the effect of the $h^0 H^+ H^-$ coupling is as small as the scenario I where the allowed ratio of radiative corrections can spread from -6.5% to -3% . At $\sqrt{s} = 500$ GeV, the allowed parameter λ_3 can be in the range $[-1.5, 3.5]$ and the radiative corrections start from -10% and can go up to 2% near the end point region of m_{H^\pm} . In contrast, in the case with the c.m. energy $\sqrt{s} = 1$ TeV, the allowed range of λ_3 becomes wider, it can change from -10 to 2 , which leads to a significant enhancement for the ratio of EW corrections as shown in the plot. The $h^0 H^+ H^-$ coupling can contribute through the charged scalar wave function renormalization and the triangle diagrams. The ratio of EW corrections is large and can even go up to 50% near the end point (for a charged scalar mass around $m_{H^\pm} = 500$ GeV).

For scenario III, we show the ratio of EW corrections in the lower panel of Fig. 4.2, where we

have taken into account all existing constraints on the parameter space of the IDM, especially the dark matter relic density, direct search constraints, and collider search of dark matter candidates. We can see that at $\sqrt{s} = 250$ GeV the dark matter constraints shrink the allowed range of λ_3 and the ratio of EW corrections can only vary between -6% and -4.8% . At $\sqrt{s} = 500$ GeV, the ratio of EW corrections can only be negative, and it can only change from -9% to -3% . At $\sqrt{s} = 1$ TeV, a larger theoretical parameter space can be probed. Accordingly, a wider range of λ_3 leads to a larger ratio of EW corrections, which can spread from -15% to 30% near the end point region.

When the allowed points in the parameter space are compared for scenarios II and III, it is noteworthy that the dark matter constraints can kill almost 99% points, as demonstrated in the lowest panels of Fig. 4.2, only sporadic points are allowed for scenario III.

It should be pointed out that the ratio of EW corrections could be large and can reach 20% or higher near the end point region, like in the $\sqrt{s} = 1$ TeV case, due to the small cross section, the production rate might also be small. For example, in the IDM5 case, when $m_{H^\pm} = 465$ GeV, the cross section is 2 fb or so. Nonetheless, when the integrated luminosity is large enough (in the case of 2/ab, we can have 4000 signal events), there is a chance to examine this loop induced effect if we could know the model parameters precisely from other measurements. Finally, we would like to point out that the EW corrections are rather significant for high c.m. energy $\sqrt{s} = 1$ TeV than they are for low energy cases $\sqrt{s} = 250$ TeV or 500 GeV. This is because the contributions from the boxes are rather important for high energy.

5 Benchmark points

BP	BP1	BP2	BP3	BP4	BP5	BP6
m_{H^\pm} (GeV)	116.8	123.4	209.5	243.7	295.4	472.9
m_{H^0} (GeV)	57.0	121.9	122.9	59.3	204.1	181.4
m_{A^0} (GeV)	102.3	200.0	125.2	238.3	205.7	473.5
μ_2^2 (GeV ²)	3159.5	14723.8	15037.5	3558.6	41195.9	32220.8
$\lambda_L(10^{-3})$	1.537	2.416	1.151	-0.798	7.847	11.819
λ_S	0.124	0.427	0.011	0.900	0.019	3.246
$\Omega h^2(\times 10^{-2})$	10.028	0.340	0.203	5.428	0.185	0.028
Γ_{H^\pm} (GeV)	5.87×10^{-4}	5.48×10^{-12}	6.77×10^{-2}	2.58	2.18×10^{-1}	1.86×10^1
Γ_{A^0} (GeV)	1.06×10^{-4}	1.23×10^{-2}	5.19×10^{-11}	2.00	8.85×10^{-12}	1.79×10^1
$Br(h^0 \rightarrow H^0 H^0)$	0.47%	-	-	0.10%	-	-
$Br(A^0 \rightarrow W^{\pm(*)} H^\mp)$	-	$\sim 76.5\%$	-	-	-	$\sim 0\%$
$Br(A^0 \rightarrow Z^{(*)} H^0)$	100%	$\sim 23.5\%$	100%	100%	100%	$\sim 100\%$
$Br(H^\pm \rightarrow W^{\pm(*)} A^0)$	$\sim 0\%$	-	$\sim 41.6\%$	$\sim 0\%$	$\sim 43.8\%$	-
$Br(H^\pm \rightarrow W^{\pm(*)} H^0)$	$\sim 100\%$	100%	$\sim 58.4\%$	$\sim 100\%$	$\sim 56.2\%$	100%

Table 5.1: Benchmark points consistent with collider experiments and dark matter constraints on the relic density are proposed. Decay information of H^0 , A^0 , and H^\pm are also given.

In Table 5.1 we propose six benchmark points from scenario III that are consistent with

current collider experiments and dark matter searches. It is important to mention that several constraints from current long-lived particles searches on the IDM exist in the literature [153,154]. However, we did not take them into account in the present analysis. But as it has been discussed in [53], limits from quasistable charged particle searches can be evaded if we set an upper bound on the charged scalar lifetime of $\tau \leq 10^{-7}$ s, this implies a lower bound on the total decay width of the charged scalar of $\Gamma_{H^\pm} \geq 6.582 \times 10^{-18}$ GeV, which is respected by our BPs.

It should be mentioned that we assume that IDM alone is not sufficient to accommodate the whole dark matter content of the Universe, therefore, we only demand that the relic density of IDM is smaller than the one required by experiments. As a matter of fact, there might be other extra sectors that can contribute to the relic density of the Universe but have not been taken into account in this work. One example is the right-handed neutrino sector, another possible candidate for dark matter are the axion or axionlike particles, and there could be others as well. Coupling constants and decay information are also presented in the table. In order to examine the radiative effects of weak interactions, we have deliberately proposed three BPs, i.e. BP2, BP4, and BP6, which are close to the threshold region of certain c.m. energies of 250 GeV, 500 GeV, and 1 TeV, respectively.

There are a few comments on the features of these benchmark points. (1) According to our previous findings given in [85], it is found that both A^0 and H^0 can be the dark matter candidates. For the sake of simplicity, in these BPs, we assume that the dark matter candidate is H^0 . (2) For BP2, the charged scalar has a long life time, which can trigger the signature of a displaced vertex caused by a massive charged particle. For BP3 and BP5, the A^0 has a long life time, which can trigger the signature of a displaced vertex caused by a neutral heavy particle. While for the rest of BPs, both A^0 and H^\pm can promptly decay when produced. (3) For BP1 and BP4, the extra invisible decay mode $h^0 \rightarrow H^0 H^0$ can be open, which will lead to a larger invisible decay branching for the SM-like Higgs boson. According to the CDR of CEPC [155] and a recent Monte Carlo study [156], the future Higgs factory of CEPC with $\sqrt{s} = 250$ GeV could have the potential to determine the branching fraction of the invisible decay of h^0 down to 0.3%. Therefore, it is possible to probe BP1 at the CEPC with $\sqrt{s} = 250$ GeV not only through $e^-e^+ \rightarrow H^+H^-$ but also via the process $e^-e^+ \rightarrow Zh^0$.

Another comment is on the decay widths of charged scalars. When decay widths are tiny, the narrow width approximation is appropriate, as benchmark points 1–4 and 5 are narrow enough since decay widths are only 1% of masses. For the case where decay widths are not tiny, as benchmark point 6 demonstrated, where decay width is around 4% of its mass, then the narrow width approximation might not be precise enough to describe the production H^+H^- and the consequent decay products. A better method to describe $e^+e^- \rightarrow H^+H^- \rightarrow W^+W^-H^0H^0$ is to include the decay widths of H^\pm in the matrix elements, instead of producing $e^+e^- \rightarrow H^+H^-$ and then decaying H^\pm to $W^\pm H^0$. Nonetheless, when its decay width is 10% smaller than its mass, our numerical calculation demonstrate, the difference is acceptable. Only when its decay width is too big, say larger than 20%, the cross section in this case should be computed carefully. Furthermore, we have explored the dependence of the decay width on the charged scalar mass, and we have found that the total decay width of the charged scalar over its mass in scenario III cannot exceed 5%.

In Table 5.2, weak corrections, QED corrections, the LO and full one-loop cross sections of these BPs are provided. Generally speaking, at $\sqrt{s} = 250$ GeV and $\sqrt{s} = 500$ GeV, the weak corrections are negative since the size (absolute value) of the $\lambda_{h^0 H^+ H^-}$ coupling is small (say from -1.5 to 1.5), as shown in Fig. 4.2. Only when the charged scalar is heavy enough (say 450 to 500 GeV) and the absolute value of the $\lambda_{h^0 H^+ H^-}$ coupling can be large (say from -10 to 2

for scenario II and from -8 to 1 for scenario III), the weak corrections Δ_{weak} can be positive when the masses of charged scalar are close to the threshold region when $\sqrt{s} = 1000$ GeV, as demonstrated by BP6. It should be mentioned that the positive contribution comes from diagrams with charged scalars in the loop.

\sqrt{s} (GeV)	BP	σ^0 (fb)	$\Delta_{\text{weak}}(\%)$	$\Delta_{\text{QED}}(\%)$	σ^{NLO} (fb)
250	BP1	23.940	-5.941	-0.138	22.484
	BP2	2.300	-4.825	-0.475	2.178
500	BP1	86.733	-7.267	0.261	80.655
	BP2	82.604	-6.373	0.247	77.543
	BP3	20.593	-9.213	0.033	18.703
	BP4	1.446	-2.842	-0.332	1.400
1000	BP1	28.563	-10.631	0.421	25.647
	BP2	28.280	-9.360	0.409	25.749
	BP3	23.284	-13.896	0.286	20.115
	BP4	20.715	-10.987	0.249	18.491
	BP5	16.365	-14.023	0.194	14.102
	BP6	1.092	11.543	-0.174	1.216

Table 5.2: Weak corrections, QED corrections, the LO and full one-loop cross sections of BPs are provided.

From the above table, one can see that at the e^+e^- colliders, in BP1, BP2, BP4 and BP6, $e^+e^- \rightarrow H^+H^-$ would lead to $W^+W^-H^0H^0$ final state, which in turn could lead to a final state with dileptons and missing energy. While for BP3 and BP5 one could have the following final states: $H^+H^- \rightarrow W^+W^-H^0H^0$ or $H^+H^- \rightarrow W^+W^-H^0A^0 \rightarrow W^+W^-Z^0H^0H^0$, which could give dilepton events as well as multileptons.

At the LHC, the situation is slightly different because we have the following production mechanisms for charged scalar: $pp \rightarrow H^+H^-$, $pp \rightarrow H^+H^0$, and $pp \rightarrow H^+A^0$. For the charged scalar pair production, similar final states as for $e^+e^- \rightarrow H^+H^-$ can be obtained. While the process $pp \rightarrow H^+H^0$ (respectively, $pp \rightarrow H^+A^0$) would give $W^+H^0H^0$ (respectively, $W^+H^0A^0 \rightarrow W^+Z^0H^0H^0$), or $W^+A^0H^0 \rightarrow W^+Z^0H^0H^0$ (respectively, $W^+A^0A^0 \rightarrow W^+Z^0Z^0H^0H^0$), which leads to final states with single/multileptons and missing energy. At the LHC, it should be pointed out that in order to pinpoint the electroweak corrections, the QCD corrections should first be reliably calculated, which are typically quite large.

Moreover, there are two more comments on our BPs: (1) We have checked our BPs in Table 5.1 and confirmed that they can survive even in light of the new direct detection results from the LUX-ZEPLIN Experiment [157]. (2) For multicomponent dark matter situations, a scaling factor is included in Ref. [56]; however, this factor is not taken into account in our work. Such a factor will ease the restrictions from direct search because we require that the relic density from IDM is not greater than the one from *Planck* data. Based on the fact that our BPs have already passed all the constraints in our analysis, it is easy to conclude that they will all survive if the factor is included.

6 Conclusions and discussions

IDM is a simple model that can solve the problem of dark matter. Such a model predicts a charged scalar in its spectrum. The observation of such charged scalar either at LHC or at the future e^+e^- colliders would be a conclusive evidence of physics beyond SM.

Future e^+e^- colliders would provide an opportunity to measure the charged scalar cross section and its properties precisely. Following the standard renormalization scheme of the SM, in this work, we study the radiative corrections of the new physics process $e^-e^+ \rightarrow H^+H^-$ in the IDM. The dimensional regularization is used to evaluate the one-loop Feynman amplitudes in the Feynman-'t Hooft gauge. We employed comprehensive on-shell scheme renormalization, which means that not only the particle masses and fields, but also the coupling constant, were renormalized using on-shell conditions. As a consequence, our predictions are totally independent of the renormalization scale μ_r . Nevertheless, a new scale m_Z is introduced via Eq. (22) where the large logarithms from light fermions are absorbed into the redefinition of the running coupling constant. The running coupling constant is changed from $1/137.036$ to $1/128.943$ correspondingly. This yields a 13% difference in the LO predictions. But this new scale dependence is greatly reduced at the NLO.

We have considered the QED corrections and checked that the IR divergences cancel when we add the virtual and real photon emissions. We have also used the resummed cross section to cure the well known Coulomb singularity. In addition, collinear divergences in our calculation appear as terms proportional to $\log(m_e)$. After including the counter term from the structure function of an electron, such divergent terms should vanish in the final result. In order to check this, we vary the mass of the electron by a factor of k from 2^{-6} to 2^6 , namely m_e is taken $k \times 0.511$ MeV. It is found that the result remains unchanged when k varies.

We have examined the size of the weak corrections for three representative c.m. energies: $\sqrt{s} = 250$, $\sqrt{s} = 500$, and $\sqrt{s} = 1000$ GeV. After taking into account the theoretical constraints and experimental bounds for the scenario III, we have found that the weak corrections are still sizable; i.e. the weak corrections are around $-6\% \sim -5\%$ for $\sqrt{s} = 250$ GeV, $-10\% \sim -3\%$ for $\sqrt{s} = 500$ GeV, and $-15\% \sim +25\%$ for $\sqrt{s} = 1000$ GeV, as shown in Fig. 4.2. The origin of those sizable corrections is the $h^0 H^+ H^-$ coupling which could become large for some configuration of the parameters. We have shown that the size of the radiative corrections, are typically of the order 5–25%, which makes their proper inclusion in any phenomenological studies and analyses for e^+e^- colliders indispensable.

From those allowed parameter points, we have proposed six benchmark points as given in Table 5.1 for future lepton collider searches. We provide the parameters, the total decay width, as well as the branching fractions of the neutral and charged scalars. According to those BPs, we have also discussed the signature of $e^+e^- \rightarrow H^+H^-$ followed by the charged scalar decays and show that it would lead to a final state with multileptons and missing energy. At the LHC, one can get similar signatures through $pp \rightarrow H^\pm H^\mp; H^\pm A^0; H^\pm H^0$ production.

It was noteworthy that initial state radiation can reduce the production rate of the process $e^+e^- \rightarrow Zh^0$ for $\sqrt{s} = 240/250$ GeV by a factor of 10% or so [158], according to the simulation done with the public code WHIZARD [159]. For the process $e^+e^- \rightarrow H^+H^-$, the NLO cross section σ^1 satisfies $\sigma^1 = |M^0 + M^1|^2 \approx |M^0|^2 + 2\text{Re}(M^0 M^{1*})$, hence the initial state and final state radiations are simply linearly summed in the matrix element of M^1 . Therefore, at the $O(\alpha)$ order, the initial state radiation of the process $e^+e^- \rightarrow H^+H^-$ is just the same as that of the process $e^+e^- \rightarrow Zh^0$, i.e., such a reduction in the production rate also holds for the process $e^+e^- \rightarrow H^+H^-$ for $\sqrt{s} = 240/250$ GeV. The reduction can be around -10% in the M_Z scheme,

as shown in Ref. [160] for $\sqrt{s} = 240$ GeV. While for the cases $\sqrt{s} = 500$ GeV and $\sqrt{s} = 1$ TeV, due to the effects of radiative return [161–163], it is expected that the initial state radiation can enhance the cross section of $e^+e^- \rightarrow H^+H^-$ when m_{H^\pm} is small, as in the cases of BP1 and BP2.

Meanwhile, at the $O(\alpha)$ order, the initial state radiation and final state radiation can be treated individually. In order to cure the Coulomb singularity arising from the final state interaction, the final state radiations can be partially resummed, and the cross section can be modified as given in Eq. (37). In terms of our numerical results given in Table 3.1, the Coulomb singularity can be reliably removed. And the resummation effect is represented by the factor $|\phi(0)|^2$. Thus the final state radiation can be correctly evaluated, which can increase the total cross section by a factor from 1% to 49%. It reaches its maximum when the invariant mass of the pair of charged scalar approaches the total collision energy, as shown in Table 3.1 for $\sqrt{s} = 500$ GeV.

For higher order $O(\alpha)$ corrections, there exist interference terms between initial state radiation and final state radiation, appropriate treatment of these two radiations is beyond the scope of current work.

Acknowledgements

We thank Jianxiong Wang for helpful discussions about FDC program. Q. S. Y. is supported by the Natural Science Foundation of China under the grant No. 11475180 and No. 11875260. B. G. is supported by the Natural Science Foundation of China Grants No. 11475183, No. 11975242, and No. 12135013. J. E. F. would like to thank the HECAP section of the Abdus Salam International Centre for Theoretical Physics (ICTP) for hospitality and financial support where part of this work has been done. The work of H. A, A. A, and J. E. F. is supported by the Moroccan Ministry of Higher Education and Scientific Research MESRSFC and CNRST: Projet PPR/2015/6.

A Details about the renormalization of charge

As mentioned in the main text, we have used an “on-shell” renormalization scheme not only for the masses and fields of particles but also for the charge. By adopting this approach, our results are independent of the renormalization scale μ_r . However, in order to resum the large logarithms arising from light fermions vacuum polarization, a new scale $Q = m_Z$ is introduced. Further details are presented below.

The electric charge renormalization is carried out following Refs. [134, 135]. The renormalization constant is obtained in the Thomson limit with the condition by imposing the condition

$$\bar{u}(p)\hat{\Gamma}_\mu^{ee\gamma}(p,p)u(p)|_{p^2=m_e^2} = ie\bar{u}(p)\gamma_\mu u(p), \quad (42)$$

which gives

$$\delta Z_e(0) = -\frac{1}{2}\delta Z_{AA} - \frac{s_W}{c_W}\frac{1}{2}\delta Z_{ZA} = \frac{1}{2}\Pi(0) - \frac{s_W}{c_W}\frac{\sum_T^{AZ}(0)}{m_Z^2} \quad (43)$$

where the renormalization constants are defined as follows (bare quantities are denoted by a subscript “0”):

$$e_0\mu^\varepsilon = Z_e e \mu_r^\varepsilon = (1 + \delta Z_e) e \mu_r^\varepsilon, \quad (44)$$

$$\begin{pmatrix} Z \\ A \end{pmatrix}_0 = \begin{pmatrix} 1 + \frac{1}{2}\delta Z_{ZZ} & \frac{1}{2}\delta Z_{ZA} \\ \frac{1}{2}\delta Z_{AZ} & 1 + \frac{1}{2}\delta Z_{AA} \end{pmatrix} \begin{pmatrix} Z \\ A \end{pmatrix}.$$

Here $\varepsilon \equiv (4 - D)/2$ with D being the space-time dimension, μ is the arbitrary mass parameter introduced for bare charge, μ_r is the renormalization scale of charge, e_0 is the bare dimensionless charge and e is the renormalized one. For the remaining quantities in Eq. (43), “ Π ” is defined as

$$\Pi(k^2) \equiv \frac{\sum_T^{AA}(k^2)}{k^2}, \quad \Pi(0) = \lim_{k^2 \rightarrow 0} \frac{\sum_T^{AA}(k^2)}{k^2} = \left. \frac{\partial \sum_T^{AA}(k^2)}{\partial k^2} \right|_{k^2=0}, \quad (45)$$

and $\sum_T^{AA(AZ)}$ denotes the transverse part of the $AA(AZ)$ self-energy. This is just the “zero-momentum” scheme in Ref. [152].

It should be noted that in the calculation of $\Pi(0)$, nonperturbative strong interaction effects cannot be neglected. In order to treat them properly, we first introduce a universal quantity:

$$\Delta\alpha(Q) \equiv \Pi(0) - \text{Re}\Pi(Q^2) \quad (46)$$

to denote the difference of Π s when the external photon is on shell and off shell, respectively. Here Q satisfies $Q^2 = k^2$ where k is the momentum of an off-shell external photon. At the one-loop level, it is easy to separate this $\Delta\alpha$ into several parts according to the particles inside the photon’s self energy, i.e.

$$\Delta\alpha = (\Delta\alpha)_f + (\Delta\alpha)_b \quad (47)$$

where the labels “ f ” and “ b ” are used to denote the contributions from fermions and bosons. For the convenience of discussion below, the $(\Delta\alpha)_f$ part can further be expressed as

$$(\Delta\alpha)_f = (\Delta\alpha)_\ell + (\Delta\alpha)_q^{(5)} + (\Delta\alpha)_{\text{top}} \quad (48)$$

and the labels “ ℓ ”, “ q ”, and “top” are used to denote the contributions from leptons, light quarks and top quarks, respectively. Here “5” in $(\Delta\alpha)_q^{(5)}$ refers to the number of quark flavors. Π can also be separated in the same way, so we will also apply the labels to Π .

Since we are trying to treat the nonperturbative effects in $\Pi(0)$, we focus on the “ q ” part here, which can be expressed as

$$(\Delta\alpha)_q^{(5)}(Q) = \Pi_q^{(5)}(0) - \text{Re}\Pi_q^{(5)}(Q^2). \quad (49)$$

Although $\Pi_q^{(5)}(0)$ can be calculated perturbatively, it is unreliable due to its nonperturbative nature at low energy regions. Hence we try to extract it from data. At the scale $Q = m_Z$, the lhs of Eq. (49) can be obtained from experiment measurements using the dispersion relation, i.e.

$$(\Delta\alpha)_q^{(5)}(m_Z) = (\Delta\alpha)_{\text{hadron}}^{(5)}(m_Z). \quad (50)$$

Here $(\Delta\alpha)_{\text{hadron}}^{(5)}(m_Z)$ is the experimental data and its value can be found from PDG [120] as $\Delta\alpha_{\text{hadron}}^{(5)}(m_Z) = 0.02764$. Meanwhile at this scale $\Pi_q^{(5)}(m_Z^2)$, the second term on the rhs of

Eq. (49), can be reliably computed by the perturbation expansion. Combing these with Eq. (49), we have

$$\Pi_q^{(5)}(0) = \text{Re}\Pi_q^{(5)}(m_Z^2) + \Delta\alpha_{\text{hadron}}^{(5)}(m_Z), \quad (51)$$

in which the nonperturbative effects have been properly included. Then $\Pi(0)$ is obtained as

$$\Pi(0) = \Pi_q^{(5)}(0) + \Pi_{\text{rest}}(0) = \text{Re}\Pi_q^{(5)}(m_Z^2) + \Delta\alpha_{\text{hadron}}^{(5)}(m_Z) + \Pi_{\text{rest}}(0). \quad (52)$$

Here “rest” denotes the contribution of “ ℓ ”, “top”, and “ b ” parts.

Once $\Pi(0)$ is determined by Eq. (52), the renormalization of charge defined by Eq. (43) corresponds to the electromagnetic fine-structure constant obtained in the Thomson limit: $\alpha(0) = 1/137.036$.

As pointed out in Sec. 8.2.1 of Ref. [134], the above renormalization of charge [labeled as $\alpha(0)$ scheme for convenience] is carried out at zero momentum transfer, where the relevant scale is set by the masses of fermions. They are much smaller than the relevant scales in high energy experiments. Hence, when working on processes in high energy experiments, such as this work, the large ratio of these different scales will cause large logarithms. These large logarithms can be summarized in the universal quantity introduced above, $\Delta\alpha(Q)$.

The leading logarithms in $\Delta\alpha$ arise from fermionic contributions and can be correctly resummed to all orders in perturbative theory by the replacement:

$$1 + (\Delta\alpha)_{\text{LL}} \rightarrow \frac{1}{1 - (\Delta\alpha)_{\text{LL}}}, \quad (53)$$

where a label “LL” is used to denotes the leading logarithms.

Meanwhile, since not only the leading logarithms but also the whole fermionic contributions are gauge invariant, we can resum the latter, i.e.

$$1 + \Delta\alpha = 1 + (\Delta\alpha)_f + (\Delta\alpha)_b \rightarrow \frac{1}{1 - (\Delta\alpha)_f} + (\Delta\alpha)_b. \quad (54)$$

On the other hand, the large logarithms in $\Delta\alpha$ originate from the renormalization constant $\delta Z_e(0)$ given in Eq. (43); hence they will appear wherever α appears in lowest order and can be taken into account by replacing the lowest order α by a running $\alpha(Q)$ as

$$\alpha_{\text{lowest}} = \alpha(0) \rightarrow \alpha(Q) = \frac{\alpha(0)}{1 - (\Delta\alpha(Q))_f}. \quad (55)$$

Here a subscript “lowest” is used to denote the lowest order α . This replacement can be taken as an effective renormalization of α at momentum transfer Q^2 . More details about this part can be found in Refs. [134, 135]. In our work, we set the relevant scale Q to m_Z and resum over the contribution from light fermions, namely the running coupling constant is defined as

$$\alpha(m_Z) = \frac{\alpha(0)}{1 - (\Delta\alpha(m_Z))_{f \neq \text{top}}}, \quad (56)$$

Here the label “ $f \neq \text{top}$ ” denotes the contributions from light fermions, which are just the sum of $(\Delta\alpha)_{\text{lepton}}$ and $(\Delta\alpha)_q^{(5)}$ in Eq. (48). This is how our $\alpha(m_Z)$ scheme is introduced. And it is regarded as an “on-shell” definition of the running coupling constant at the scale m_Z following

the notation in PDG [120]. Corresponding renormalization constants can be derived easily with Eq. (56), which is

$$\delta Z_e(m_Z) = \delta Z_e(0) - \frac{1}{2}(\Delta\alpha(m_Z))_{f \neq \text{top}}. \quad (57)$$

The above discussion is based on our choice of physical parametrization, $\{\alpha, m_W, m_Z\}$. Sometimes people use the Fermi constant G_F as an input. Here we try to discuss the uncertainties arising from different input schemes. The relationship between G_F and above parameters is already well known, which is

$$G_F = \frac{\pi\alpha(1 + \Delta r)}{\sqrt{2}m_W^2 \left(1 - \frac{m_W^2}{m_Z^2}\right)}. \quad (58)$$

Δr can be calculated perturbatively. It vanishes at LO and its expression at NLO can be found in Ref. [134]. Here we take G_F as an observable, which is used to extract the value of certain renormalized physical parameter(s). The renormalization scheme in this case is exactly the same as the $\alpha(0)$ scheme.

If the input scheme is $\{\alpha, G_F, m_Z\}$, then this means the mass of W boson has to be extracted with Eq. (58). However, there are some difficulties in this extraction:

1. There are new physics contributions in Δr , which make it vary in the IDM parameter space.
2. Δr itself also depends on m_W .

Hence, we use its SM value $\Delta r = 0.03652$ [120] as an approximation to estimate m_W , which leads to

$$m_W = m_Z \sqrt{\frac{1}{2} + \sqrt{\frac{1}{4} - \frac{\pi\alpha(1 + \Delta r)}{\sqrt{2}G_F m_Z^2}}} \approx 80.382 \text{ GeV}. \quad (59)$$

It is very close to the value of m_W we use in the $\{\alpha, m_W, m_Z\}$ scheme, which means the four inputs are precisely consistent. This indicates that the difference between these two schemes is negligible.

If the input scheme is $\{G_F, m_W, m_Z\}$, then the situation is similar, since we have verified the consistency of the four inputs. However, in this case, similar to what we have done in Eq. (55), we can introduce another effective coupling constant, which is

$$\alpha_{G_F} = \frac{\alpha}{1 - \Delta r} \approx \alpha(1 + \Delta r). \quad (60)$$

The value of α_{G_F} can be obtained directly from Eq. (58), with no more approximation. We replace all the α with this α_{G_F} in our calculation. This can also be taken as an effective renormalization of α , with the renormalization constant

$$\delta Z_e|_{G_F} = \delta Z_e(0) - \frac{1}{2}\Delta r. \quad (61)$$

Since Δr also contains $\Pi(0)$, it will cancel with the one in $\delta Z_e(0)$. Hence $\delta Z_e|_{G_F}$ no longer contains $\Pi(0)$, and the large logarithms discussed above are also resummed in this α_{G_F} scheme.

Case	1	2	3	4	5
Input	$\{\alpha, m_W, m_Z\}$	$\{\alpha, m_W, m_Z\}$	$\{\alpha, G_F, m_Z\}$	$\{G_F, m_W, m_Z\}$	$\{G_F, m_W, m_Z\}$
Renormalization	$\alpha(0)$	$\alpha(m_Z)$	$\alpha(0)$	$\alpha(0)$	α_{G_F}

Table A.1: Several cases with different input and renormalization schemes are defined.

We list all the cases discussed above in Table A.1. Cases 3 and 4 are very similar to case 1 due to the precise consistency among the four inputs. Hence, we skip them and consider the others. We choose a certain point in the IDM parameter space and calculate the cross section in three renormalization schemes. The results are shown in Table A.2. It can be observed that scheme dependence is greatly reduced at the NLO. However, it should be pointed out that the difference in the relative corrections is quite large, which originates from the difference in the LO results. Hence, when focusing on relative corrections, the difference in the LO results should be considered. And this can be easily estimated by the values of α in the table. For example, the relative correction in $\alpha(m_Z)$ scheme can be converted to $\alpha(0)$ (α_{G_F}) scheme approximately by adding an extra piece of 12.9% (5.1%). After this, it can be seen that the difference in the remaining parts is around 1%, and is consistent with the difference in the NLO cross sections.

Case	Scheme	α^{-1}	σ^0	σ_{QED}^1	σ_{WEAK}^1	σ^1	σ^{NLO}	$\Delta(\%)$
1	$\alpha(0)$	137.036	23.678	0.468	1.528	1.996	25.674	8.43
2	$\alpha(m_Z)$	128.943	26.744	0.562	-1.523	-0.961	25.783	-3.59
5	α_{G_F}	132.184	25.448	0.522	0.128	0.650	26.098	2.55

Table A.2: Cross sections and relative corrections in different renormalization schemes are presented. The unit of cross sections is fb. IDM parameters are chosen as $m_H = m_A = m_{H^\pm} = 200$ GeV, $\lambda_2 = 2$, and $\mu_2^2 = 0$. Values of the four inputs are taken as $\alpha(0) = 1/137.036$, $m_W = 80.379$ GeV, $m_Z = 91.1876$ GeV, and $G_F = 1.1663787 \times 10^{-5}$ GeV $^{-2}$.

B Wave function renormalization

At the end of this section, we provide the explicit expression for δZ_{H^\pm} , the only needed renormalization constant from the inert section in this work. It can be separated into four parts according to the boson inside the self-energy, namely

$$\delta Z_{H^\pm} = \delta Z_{H^\pm}^{W/G} + \delta Z_{H^\pm}^{Z/G} + \delta Z_{H^\pm}^\gamma + \delta Z_{H^\pm}^h, \quad (62)$$

with

$$\begin{aligned}
\delta Z_{H^\pm}^{W/G} &= \frac{\alpha}{4\pi} \times \frac{1}{4s_W^2} \{ (B_0[m_{H^\pm}^2, m_{A^0}^2, m_W^2] + B_0[m_{H^\pm}^2, m_{H^0}^2, m_W^2]) \\
&\quad - 2(B_1[m_{H^\pm}^2, m_{A^0}^2, m_W^2] + B_1[m_{H^\pm}^2, m_{H^0}^2, m_W^2]) \\
&\quad - 2m_{H^\pm}^2 (B'_1[m_{H^\pm}^2, m_{A^0}^2, m_W^2] + B'_1[m_{H^\pm}^2, m_{H^0}^2, m_W^2]) \\
&\quad + [(m_{A^0}^2 + m_{H^\pm}^2) - (m_{A^0}^2 - m_{H^\pm}^2)^2/m_W^2] B'_0[m_{H^\pm}^2, m_{A^0}^2, m_W^2] \\
&\quad + [(m_{H^0}^2 + m_{H^\pm}^2) - (m_{H^0}^2 - m_{H^\pm}^2)^2/m_W^2] B'_0[m_{H^\pm}^2, m_{H^0}^2, m_W^2] \} \\
\delta Z_{H^\pm}^{Z/G} &= \frac{\alpha}{4\pi} \times g_H^2 \{ B_0[m_{H^\pm}^2, m_{H^\pm}^2, m_Z^2] - 2B_1[m_{H^\pm}^2, m_{H^\pm}^2, m_Z^2] \\
&\quad + 2m_{H^\pm}^2 B'_0[m_{H^\pm}^2, m_{H^\pm}^2, m_Z^2] - 2m_{H^\pm}^2 B'_1[m_{H^\pm}^2, m_{H^\pm}^2, m_Z^2] \} \\
\delta Z_{H^\pm}^\gamma &= \frac{\alpha}{4\pi} \times \{ B_0[m_{H^\pm}^2, 0, m_{H^\pm}^2] - 2B_1[m_{H^\pm}^2, m_{H^\pm}^2, 0] \\
&\quad + 2m_{H^\pm}^2 B'_0[m_{H^\pm}^2, 0, m_{H^\pm}^2] - 2m_{H^\pm}^2 B'_1[m_{H^\pm}^2, m_{H^\pm}^2, 0] \} \\
\delta Z_{H^\pm}^h &= \frac{\alpha}{4\pi} \times \frac{-(m_{H^\pm}^2 - \mu_2^2)^2}{m_W^2 s_W^2} B'_0[m_{H^\pm}^2, m_{h^0}^2, m_{H^\pm}^2]
\end{aligned} \tag{63}$$

and

$$B'_i[m_{H^\pm}^2, m_1^2, m_2^2] \equiv \left. \frac{\partial B_i[k^2, m_1^2, m_2^2]}{\partial k^2} \right|_{k^2=m_{H^\pm}^2}. \tag{64}$$

Here the two-point functions B_0 and B_1 are defined as

$$\begin{aligned}
B_0[p_1^2, m_1^2, m_2^2] &= \frac{(2\pi\mu_r)^{4-D}}{i\pi^2} \int d^D q \frac{1}{(q^2 - m_1^2)((q + p_1)^2 - m_2^2)} \\
B_1[p_1^2, m_1^2, m_2^2] &= \frac{1}{2} \left\{ A_0[m_1^2] - A_0[m_2^2] - [p_1^2 + m_1^2 - m_2^2] B_0[p_1^2, m_1^2, m_2^2] \right\}
\end{aligned} \tag{65}$$

with μ_r being the renormalization scale and A_0 being the one-point function given by

$$A_0(m_1^2) = \frac{(2\pi\mu_r)^{4-D}}{i\pi^2} \int d^D q \frac{1}{q^2 - m_1^2}. \tag{66}$$

In our work, as shown in Eq. (44), the mass parameter μ in bare charge is replaced by μ_r after the renormalization. Consequently, μ_r appears instead of μ in above one- and two-point functions.

C More details about treatment on IR divergences

As mentioned in the main text, IR divergences in this work are regularized with a small fictitious photon mass λ . Meanwhile, two cutoffs, ΔE and $\Delta\theta$, are introduced to deal with the IR singularities in real correction processes based on the two cutoff phase space slicing method [139]. The three-body phase space of the real correction process $e^+e^- \rightarrow H^+H^-\gamma$ is then divided into three parts:

- Soft (S) part: Where the energy of photon E_γ is smaller than ΔE .
- Hard collinear (HC) part: Where $E_\gamma \geq \Delta E$ and the angle between photon and the beam θ_γ is smaller than $\Delta\theta$.

- Hard noncollinear ($H\overline{C}$) part: The remaining, which is finite.

The full NLO corrections are then separated into four parts, as given in Eq. (67):

$$d\sigma^1 = d\sigma_V(\lambda) + d\sigma_S(\lambda, \Delta E) + d\sigma_{HC+CT}(\Delta E, \Delta\theta) + d\sigma_{H\overline{C}}(\Delta E, \Delta\theta) \quad (67)$$

Here $d\sigma_V$ denotes the virtual correction, including loop diagrams and counter terms from renormalization. And CT in the third term of rhs denotes the extra contribution arising from the structure function of the incoming electron and positron.

In our work, the first two parts, $d\sigma_V$ and $d\sigma_S$, are obtained using **FeynArts** and **FormCalc** [145–147] packages, in which numerical evaluations of the scalar integrals are done with **LoopTools** [148, 149]. The other two parts, $d\sigma_{HC+CT}$ and $d\sigma_{H\overline{C}}$, are obtained with the help of **FDC** [150] and **BASES** [151].

The soft part is calculated in the soft limit. After the phase space integration of the soft photon, it can be expressed as the product of a factor and the LO result. The result of this part can be found in the literature [102, 106]. For completeness, we give the analytical expressions here:

$$\begin{aligned} d\sigma_S = -\frac{\alpha}{\pi} d\sigma^0 \times & \left\{ 4 \log \frac{2\Delta E}{\lambda} - 2 \log \frac{2\Delta E}{\lambda} \log \frac{s}{m_e^2} + \log \frac{m_e^2}{s} + \frac{\pi^2}{3} + \frac{1}{2} \log^2 \frac{m_e^2}{s} \right. \\ & + \frac{1+\beta^2}{\beta} \log \frac{2\Delta E}{\lambda} \log \left(\frac{1-\beta}{1+\beta} \right) + \frac{1}{\beta} \log \left(\frac{1-\beta}{1+\beta} \right) + \frac{1+\beta^2}{\beta} \left[\text{Li}_2 \left(\frac{2\beta}{1+\beta} \right) + \log^2 \left(\frac{1-\beta}{1+\beta} \right) \right] \\ & + 4 \log \frac{2\Delta E}{\lambda} \log \frac{m_{H^\pm}^2 - u}{m_{H^\pm}^2 - t} + 2 \left[\text{Li}_2 \left(1 - \frac{s(1-\beta)}{2(m_{H^\pm}^2 - t)} \right) + \text{Li}_2 \left(1 - \frac{s(1+\beta)}{2(m_{H^\pm}^2 - t)} \right) \right. \\ & \left. \left. - \text{Li}_2 \left(1 - \frac{s(1-\beta)}{2(m_{H^\pm}^2 - u)} \right) - \text{Li}_2 \left(1 - \frac{s(1+\beta)}{2(m_{H^\pm}^2 - u)} \right) \right] \right\} \end{aligned} \quad (68)$$

where Li_2 represents the known dilogarithm function. **FormCalc** has the option to include soft bremsstrahlung automatically when calculating the virtual corrections. We have confirmed that the results from **FormCalc** are consistent with the above expression. Meanwhile, by varying the value of λ inside **FormCalc**, we confirm the λ independence of our results.

The hard noncollinear part, $d\sigma_{H\overline{C}}$, needs no more special treatment. It is obtained using traditional Monte Carlo integration techniques with the **FDC** package, in which **BASES** [151] is used for multidimensional numerical integration.

The hard collinear part is obtained in the collinear limit as

$$d\sigma_{HC} = \frac{\alpha}{2\pi} \left[\frac{1+z^2}{1-z} \log \frac{\Delta\theta^2 + 4m_e^2/s}{4m_e^2/s} - \frac{2z}{1-z} \frac{\Delta\theta^2}{\Delta\theta^2 + 4m_e^2/s} \right] d\sigma^0(zp_1) dz + (p_1 \leftrightarrow p_2) \quad (69)$$

Here z denotes the energy fraction of the electron (positron) after the emission of collinear a photon; hence, $0 \leq z \leq 1 - \delta_s$. We have used a dimensionless parameter $\delta_s = 2\Delta E/\sqrt{s}$ to replace ΔE . We have used $d\sigma^0 \equiv d\sigma^0(p_1, p_2)$, $d\sigma^0(zp_1) \equiv d\sigma^0(zp_1, p_2)$, and $d\sigma^0(zp_2) \equiv d\sigma^0(p_1, zp_2)$ for convenience.

It is found that in the limit $\Delta\theta^2 \gg m_e^2/s$, the hard collinear part given in Eq. (69) can be expressed in a simpler form as given below

$$d\sigma_{HC} \xrightarrow{\Delta\theta^2 \gg m_e^2/s} \frac{\alpha}{2\pi} \left[\frac{1+z^2}{1-z} \log \frac{\Delta\theta^2 s}{4m_e^2} - \frac{2z}{1-z} \right] \times \left[d\sigma^0(zp_1) + d\sigma^0(zp_2) \right] dz. \quad (70)$$

We will use the form given in Eq. (70) as our default formula to compute the full cross section given in Eq. (67). It is interesting to explore the difference between the results of Eq. (69) and Eq. (70), and we will explore this issue near the end of this section.

One-loop radiation correction includes collinear singularities, which lead to terms proportional to $\log(m_e)$. Some of them are canceled when summing up virtual and real corrections. Some of them are absorbed into the redefinition of the running coupling constant, as shown in Eq. (56). But there are still some remaining. To deal with this, the structure function approach [164] is applied. According to the approach, the cross section of e^+e^- annihilation can be expressed as

$$d\bar{\sigma}_{e^+e^-}(p_1, p_2) = \sum_{ij} dx_1 dx_2 f_{ie^+}(x_1, \bar{Q}^2) f_{je^-}(x_2, \bar{Q}^2) d\sigma_{ij}(x_1 p_1, x_2 p_2) \quad (71)$$

Here $f_{ia}(x, \bar{Q}^2)$ is the so-called structure function, which denotes the possibility to find parton i with energy fraction x from particle a at scale \bar{Q} . In Eq. (71), all remaining collinear singularities are absorbed into the structure functions and resummed there. The parton-level cross section $d\sigma_{ij}$ is then free of those large logarithms. The particle-level cross section $d\bar{\sigma}_{e^+e^-}$ is obtained by convoluting the partonic cross section with the structure functions. This factorization theorem is extended from QCD with $i, a \in \{e^+, e^-, \gamma\}$. Strictly speaking, what we are studying in this work is the parton-level cross section of H^+H^- production only. Since we are interested in the NLO corrections in the whole parameter space, this is sufficient. But if we want to study the exact cross section of production, convolution with the structure functions is needed.

In QED, all the structure functions $f_{ia}(x, \bar{Q}^2)$ are perturbatively calculable. They can be expanded into a series of α , namely

$$f_{ia}(x, \bar{Q}^2) = f_{ia}^0(x, \bar{Q}^2) + f_{ia}^1(x, \bar{Q}^2) + \mathcal{O}(\alpha^2), \quad (72)$$

Meanwhile it is obvious that the first term in above expansion always takes the form

$$f_{ia}^0(x, \bar{Q}^2) = \delta(1-x)\delta_{ia}. \quad (73)$$

Based on this, in this work up to one-loop level, Eq. (71) can be rewritten into (using $f_{ee} \equiv f_{e^-e^-} = f_{e^+e^+}$)

$$d\bar{\sigma}_{e^+e^-}(p_1, p_2) = dx_1 dx_2 f_{ee}(x_1, \bar{Q}^2) f_{ee}(x_2, \bar{Q}^2) d\sigma_{e^+e^-}(x_1 p_1, x_2 p_2) \quad (74)$$

Expanding both sides of Eq. (74) to NLO and applying Eq. (73), it is easy to find

$$\begin{aligned} d\bar{\sigma}_{e^+e^-}^0(p_1, p_2) &= d\sigma_{e^+e^-}^0(p_1, p_2) \\ d\bar{\sigma}_{e^+e^-}^1(p_1, p_2) &= d\sigma_{e^+e^-}^1(p_1, p_2) + dx_1 f_{ee}^1(x_1, \bar{Q}^2) d\sigma_{e^+e^-}^0(x_1 p_1, p_2) \\ &\quad + dx_2 f_{ee}^1(x_2, \bar{Q}^2) d\sigma_{e^+e^-}^0(p_1, x_2 p_2), \end{aligned} \quad (75)$$

which leads to

$$d\bar{\sigma}_{e^+e^-}^1(p_1, p_2) = d\bar{\sigma}_{e^+e^-}^1(p_1, p_2) - dz f_{ee}^1(z, \bar{Q}^2) \left[d\sigma_{e^+e^-}^0(z p_1, p_2) + d\sigma_{e^+e^-}^0(p_1, z p_2) \right] \quad (76)$$

The latter term on the rhs is just the counterterm mentioned above.

On the other hand, f_{ee} satisfies following equation [164]:

$$f_{ee}(x, \bar{Q}^2) = \delta(1-x) + \int_{m_e^2}^{\bar{Q}^2} \frac{\alpha(\bar{Q}_1^2)}{2\pi} \frac{d\bar{Q}_1^2}{\bar{Q}_1^2} \int_x^1 \frac{dz}{z} P_{ee}^+(z) f_{ee}\left(\frac{x}{z}, \bar{Q}_1^2\right), \quad (77)$$

with

$$P_{ee}^+(z) = \frac{1+z^2}{(1-z)_+} + \frac{3}{2}\delta(1-z), \quad (78)$$

being the regularized Altarelli-Parisi splitting function. This equation can be solved recursively according to the power of α , which leads to

$$f_{ee}^1(x, \bar{Q}^2) = \frac{\alpha}{2\pi} \log \frac{\bar{Q}^2}{m_e^2} P_{ee}^+(x). \quad (79)$$

In this work, the scale \bar{Q} is taken as the energy of beam in the center-of-mass frame, $\bar{Q} = \sqrt{s}/2$. The CT parts are finally obtained via Eqs. (76) and (79) as [after same notations as in Eq. (69) are taken]

$$d\sigma_{CT} = -\frac{\alpha}{2\pi} \log \frac{s}{4m_e^2} P_{ee}^+(z) \left[d\sigma^0(zp_1) + d\sigma^0(zp_2) \right] dz \quad (80)$$

with $0 \leq z \leq 1$.

The combination of $d\sigma_{HC}$ and $d\sigma_{CT}$ can be separated into two parts according to the range of z , $d\sigma_{HC+CT} = d\sigma_{HC+CT}^* + d\sigma_{SC}$. In the range $0 \leq z \leq 1 - \delta_s$, it gives

$$d\sigma_{HC+CT}^* = \frac{\alpha}{2\pi} \left[\frac{1+z^2}{1-z} \log \Delta\theta^2 - \frac{2z}{1-z} \right] \times \left[d\sigma^0(zp_1) + d\sigma^0(zp_2) \right] dz, \quad (81)$$

while in the range $1 - \delta_s \leq z \leq 1$, it gives (only $d\sigma_{CT}$ contributes to this part)

$$d\sigma_{SC} = -\frac{\alpha}{\pi} \log \frac{s}{4m_e^2} \left[\frac{3}{2} + 2 \log \delta_s \right] d\sigma^0. \quad (82)$$

Now all the parts in Eq. (67) are available.

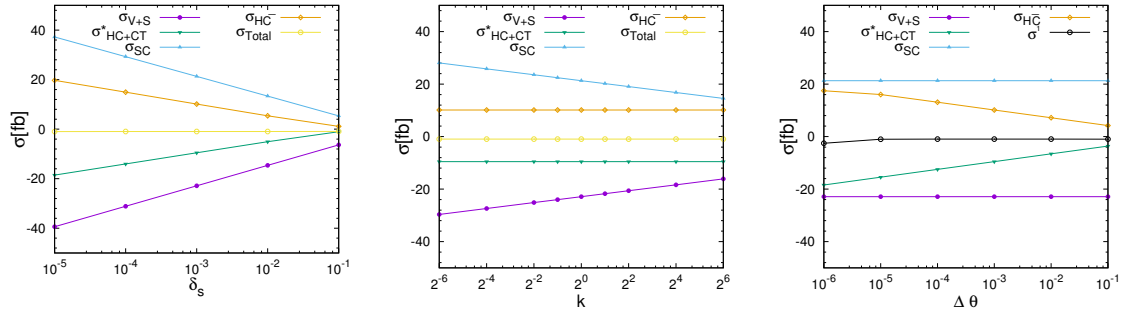


Figure C.1: One-loop corrections of $e^+e^- \rightarrow H^+H^-$ as functions of δ_s , k , and $\Delta\theta$ are demonstrated.

δ_s	σ_{V+S}	σ_{HC+CT}^*	σ_{SC}	$\sigma_{H\bar{C}}$	SUM
10^{-1}	-6.364(0)	-1.047(0)	5.371(0)	1.118(0)	-0.922(0)
10^{-2}	-14.621(0)	-5.074(1)	13.338(1)	5.399(0)	-0.958(1)
10^{-3}	-22.878(0)	-9.531(1)	21.304(1)	10.144(1)	-0.961(2)
10^{-4}	-31.135(0)	-14.031(2)	29.270(2)	14.935(1)	-0.961(3)
10^{-5}	-39.392(0)	-18.536(3)	37.237(2)	19.730(2)	-0.961(4)
k	σ_{V+S}	σ_{HC+CT}^*	σ_{SC}	$\sigma_{H\bar{C}}$	SUM
2^{-6}	-29.641(0)	-9.531(1)	28.067(2)	10.144(1)	-0.961(2)
2^{-4}	-27.387(0)	-9.531(1)	25.813(1)	10.144(1)	-0.961(2)
2^{-2}	-25.132(0)	-9.531(1)	23.558(1)	10.144(1)	-0.961(2)
2^{-1}	-24.005(0)	-9.531(1)	22.431(1)	10.144(1)	-0.961(2)
2^0	-22.878(0)	-9.531(1)	21.304(1)	10.144(1)	-0.961(2)
2^1	-21.751(0)	-9.531(1)	20.177(1)	10.144(1)	-0.961(2)
2^2	-20.624(0)	-9.531(1)	19.050(1)	10.144(1)	-0.961(2)
2^4	-18.370(0)	-9.531(1)	16.795(1)	10.144(1)	-0.962(2)
2^6	-16.115(0)	-9.531(1)	14.541(1)	10.144(1)	-0.961(2)

Table C.1: Data used in the checks on the independence of δ_s and m_e in unit of fb are shown. The third column is obtained by using Eq. (70). Numbers in the brackets are integration errors to the last digits of the data.

$\Delta\theta$	σ_{V+S}	σ_{HC+CT}^*	σ_{SC}	$\sigma_{H\bar{C}}$	SUM	$\sigma_{HC+CT}^{*,\text{origin.}}$	SUM ^{origin.}
10^{-1}	-22.878(0)	-3.605(0)	21.304(1)	4.214(0)	-0.965(1)	-3.605(0)	-0.965(1)
10^{-2}	-22.878(0)	-6.568(1)	21.304(1)	7.180(1)	-0.962(2)	-6.568(1)	-0.962(2)
10^{-3}	-22.878(0)	-9.531(1)	21.304(1)	10.144(1)	-0.961(2)	-9.531(1)	-0.961(2)
10^{-4}	-22.878(0)	-12.495(2)	21.304(1)	13.107(1)	-0.962(2)	-12.494(2)	-0.961(2)
10^{-5}	-22.878(0)	-15.458(2)	21.304(1)	16.019(1)	-1.013(2)	-15.406(2)	-0.961(2)
10^{-6}	-22.878(0)	-18.421(2)	21.304(1)	17.459(2)	-2.536(3)	-16.845(2)	-0.960(3)

Table C.2: Data used in the checks on the independence of $\Delta\theta$ in unit of fb are shown. The seventh column and the eighth column with the superscript “origin.” denote the results by using Eq. (69). In contrast, the third column and the sixth column denote the results by using Eq. (70). Numbers in the brackets are integration errors to the last digits of the data.

It should be stressed that ΔE (δ_s) and $\Delta\theta$ are unphysical cutoffs we introduced to deal with IR and collinear singularities. Our final results should not depend on them. In order to check this, we choose a certain point (same as the one used in Table A.2) in the IDM parameter space and compare the NLO corrections σ^1 obtained with different cutoffs. The results are shown in Fig. C.1, with corresponding data in Tables C.1 and C.2.

From the first subfigure, it can be seen that the independence on δ_s is found in a wide range and $\delta_s = 10^{-3}$ is used as our default choice.

Collinear divergences in our calculation appear as terms proportional to $\log(m_e)$. After including the counterterm from the structure function of an electron, such divergent terms should vanish in the final result. In order to check this, we vary the mass of the electron by a factor of k from 2^{-6} to 2^6 , namely m_e is taken $k \times 0.511$ MeV. The cancellation is shown in the second subfigure of Fig. C.1, from which we can see that the result remains unchanged as k varies. Furthermore, singular terms appear only in the σ_{V+S} and σ_{SC} parts.

In the third subfigure, we can see that the result becomes cut dependent when $\Delta\theta$ is smaller

than 10^{-4} . It can be attributed to the fact that Eq. (70) can only hold when $\Delta\theta \gg m_e/\sqrt{s} \sim 2 \times 10^{-6}$.

It is interesting to compare the results computed by using Eqs. (70) and (69), which are provided in Table C.2. It is clear that the result which is labeled by a superscript “origin.” is almost independent of the values of $\Delta\theta$ (when $\Delta\theta$ is small enough), and the difference between the results calculated by using Eqs. (70) and (69) is tiny when $\Delta\theta$ is chosen appropriately (say $\Delta\theta \sim 10^{-3}$ or larger). In our practical computation, we choose $\Delta\theta = 10^{-3}$ in this work.

In addition to the above checks for independence on λ , δ_s , $\Delta\theta$, and $\log(m_e)$, our results also passed many other self-checks:

- The IDM model used in **FDC** is generated with its own code. We have confirmed that both **FDC** and **FormCalc** give the same results at LO.
- The soft part $d\sigma_S$ has been calculated individually and checked with analytic results, as mentioned before.
- The other parts of real emission, $d\sigma_{HC+CT}$ and $d\sigma_{H\bar{C}}$, obtained with **FDC** are also tree-level calculations. This part of **FDC** has been used in many other calculations (see e.g. [165, 166]).
- **FormCalc** is a public package that has been used in many one-loop EW calculations (see e.g. [167, 168]) as well as in our previous works [85, 160].
- We have also checked our model file using the output from **FeynRules**.

However, it should be noted that further cross-checks are still important and welcome.

References

- [1] **ATLAS** Collaboration, G. Aad et al., *Observation of a new particle in the search for the Standard Model Higgs boson with the ATLAS detector at the LHC*, *Phys. Lett. B* **716** (2012) 1–29, [[arXiv:1207.7214](#)].
- [2] **CMS** Collaboration, S. Chatrchyan et al., *Observation of a new boson at a mass of 125 GeV with the CMS experiment at the LHC*, *Phys. Lett. B* **716** (2012) 30–61, [[arXiv:1207.7235](#)].
- [3] **CMS** Collaboration, A. M. Sirunyan et al., *Observation of $t\bar{t}H$ production*, *Phys. Rev. Lett.* **120** (2018), no. 23 231801, [[arXiv:1804.02610](#)].
- [4] **ATLAS** Collaboration, M. Aaboud et al., *Observation of Higgs boson production in association with a top quark pair at the LHC with the ATLAS detector*, *Phys. Lett. B* **784** (2018) 173–191, [[arXiv:1806.00425](#)].
- [5] **CMS** Collaboration, A. M. Sirunyan et al., *Observation of the Higgs boson decay to a pair of τ leptons with the CMS detector*, *Phys. Lett. B* **779** (2018) 283–316, [[arXiv:1708.00373](#)].
- [6] **ATLAS** Collaboration, M. Aaboud et al., *Cross-section measurements of the Higgs boson decaying into a pair of τ -leptons in proton-proton collisions at $\sqrt{s} = 13$ TeV with the ATLAS detector*, *Phys. Rev. D* **99** (2019) 072001, [[arXiv:1811.08856](#)].

- [7] **ATLAS** Collaboration, M. Aaboud et al., *Observation of $H \rightarrow b\bar{b}$ decays and VH production with the ATLAS detector*, *Phys. Lett. B* **786** (2018) 59–86, [[arXiv:1808.08238](#)].
- [8] **CMS** Collaboration, A. M. Sirunyan et al., *Observation of Higgs boson decay to bottom quarks*, *Phys. Rev. Lett.* **121** (2018), no. 12 121801, [[arXiv:1808.08242](#)].
- [9] **CMS** Collaboration, A. M. Sirunyan et al., *Measurement and interpretation of differential cross sections for Higgs boson production at $\sqrt{s} = 13$ TeV*, *Phys. Lett. B* **792** (2019) 369–396, [[arXiv:1812.06504](#)].
- [10] **ATLAS** Collaboration, G. Aad et al., *Measurements of Higgs boson production and couplings in diboson final states with the ATLAS detector at the LHC*, *Phys. Lett. B* **726** (2013) 88–119, [[arXiv:1307.1427](#)]. [Erratum: *Phys.Lett.B* 734, 406–406 (2014)].
- [11] **ATLAS** Collaboration, M. Aaboud et al., *Measurements of gluon-gluon fusion and vector-boson fusion Higgs boson production cross-sections in the $H \rightarrow WW^* \rightarrow e\nu\mu\nu$ decay channel in pp collisions at $\sqrt{s} = 13$ TeV with the ATLAS detector*, *Phys. Lett. B* **789** (2019) 508–529, [[arXiv:1808.09054](#)].
- [12] **ATLAS** Collaboration, G. Aad et al., *Measurement of the production cross section for a Higgs boson in association with a vector boson in the $H \rightarrow WW^* \rightarrow \ell\nu\ell\nu$ channel in pp collisions at $\sqrt{s} = 13$ TeV with the ATLAS detector*, *Phys. Lett. B* **798** (2019) 134949, [[arXiv:1903.10052](#)].
- [13] **CMS** Collaboration, A. M. Sirunyan et al., *Measurements of properties of the Higgs boson decaying to a W boson pair in pp collisions at $\sqrt{s} = 13$ TeV*, *Phys. Lett. B* **791** (2019) 96, [[arXiv:1806.05246](#)].
- [14] **CMS** Collaboration, A. M. Sirunyan et al., *Measurement of the inclusive and differential Higgs boson production cross sections in the leptonic WW decay mode at $\sqrt{s} = 13$ TeV*, *JHEP* **03** (2021) 003, [[arXiv:2007.01984](#)].
- [15] **ATLAS** Collaboration, M. Aaboud et al., *Measurements of Higgs boson properties in the diphoton decay channel with 36 fb^{-1} of pp collision data at $\sqrt{s} = 13$ TeV with the ATLAS detector*, *Phys. Rev. D* **98** (2018) 052005, [[arXiv:1802.04146](#)].
- [16] **ATLAS** Collaboration, G. Aad et al., *A search for the $Z\gamma$ decay mode of the Higgs boson in pp collisions at $\sqrt{s} = 13$ TeV with the ATLAS detector*, *Phys. Lett. B* **809** (2020) 135754, [[arXiv:2005.05382](#)].
- [17] **CMS** Collaboration, A. M. Sirunyan et al., *Search for the decay of a Higgs boson in the $\ell\ell\gamma$ channel in proton-proton collisions at $\sqrt{s} = 13$ TeV*, *JHEP* **11** (2018) 152, [[arXiv:1806.05996](#)].
- [18] **ATLAS** Collaboration, *A search for the rare decay of the Standard Model Higgs boson to dimuons in pp collisions at $\sqrt{s} = 13$ TeV with the ATLAS Detector*, .
- [19] **CMS** Collaboration, A. M. Sirunyan et al., *Search for the Higgs boson decaying to two muons in proton-proton collisions at $\sqrt{s} = 13$ TeV*, *Phys. Rev. Lett.* **122** (2019), no. 2 021801, [[arXiv:1807.06325](#)].

- [20] M. Cepeda et al., *Report from Working Group 2, CERN Yellow Rep. Monogr.* **7** (2019) 221–584, [[arXiv:1902.00134](#)].
- [21] J. de Blas et al., *Higgs Boson Studies at Future Particle Colliders*, *JHEP* **01** (2020) 139, [[arXiv:1905.03764](#)].
- [22] A. Arbey et al., *Physics at the e^+e^- Linear Collider*, *Eur. Phys. J.* **C75** (2015), no. 8 371, [[arXiv:1504.01726](#)].
- [23] P. Bambade et al., *The International Linear Collider: A Global Project*, [arXiv:1903.01629](#).
- [24] **CEPC-SPPC Study Group** Collaboration, M. Ahmad et al., *CEPC-SPPC Preliminary Conceptual Design Report. 1. Physics and Detector*, *IHEP-CEPC-DR-2015-01, IHEP-TH-2015-01, IHEP-EP-2015-01* (2015).
- [25] **CLIC Physics Working Group** Collaboration, E. Accomando et al., *Physics at the CLIC multi-TeV linear collider*, in *Proceedings, 11th International Conference on Hadron spectroscopy (Hadron 2005): Rio de Janeiro, Brazil, August 21-26, 2005*, 2004, [hep-ph/0412251](#).
- [26] M. Aicheler, P. Burrows, M. Draper, T. Garvey, P. Lebrun, K. Peach, N. Phinney, H. Schmickler, D. Schulte, and N. Toge, *A Multi-TeV Linear Collider Based on CLIC Technology*, .
- [27] L. Linssen, A. Miyamoto, M. Stanitzki, and H. Weerts, *Physics and Detectors at CLIC: CLIC Conceptual Design Report*, [arXiv:1202.5940](#).
- [28] **TLEP Design Study Working Group** Collaboration, M. Bicer et al., *First Look at the Physics Case of TLEP*, *JHEP* **01** (2014) 164, [[arXiv:1308.6176](#)].
- [29] K. Fujii et al., *Physics Case for the 250 GeV Stage of the International Linear Collider*, [arXiv:1710.07621](#).
- [30] T. D. Lee, *A Theory of Spontaneous T Violation*, *Phys. Rev. D* **8** (1973) 1226–1239.
- [31] G. C. Branco, P. M. Ferreira, L. Lavoura, M. N. Rebelo, M. Sher, and J. P. Silva, *Theory and phenomenology of two-Higgs-doublet models*, *Phys. Rept.* **516** (2012) 1–102, [[arXiv:1106.0034](#)].
- [32] N. G. Deshpande and E. Ma, *Pattern of Symmetry Breaking with Two Higgs Doublets*, *Phys. Rev.* **D18** (1978) 2574.
- [33] E. Ma, *Verifiable radiative seesaw mechanism of neutrino mass and dark matter*, *Phys. Rev.* **D73** (2006) 077301, [[hep-ph/0601225](#)].
- [34] M. Gustafsson, E. Lundstrom, L. Bergstrom, and J. Edsjo, *Significant Gamma Lines from Inert Higgs Dark Matter*, *Phys. Rev. Lett.* **99** (2007) 041301, [[astro-ph/0703512](#)].
- [35] T. Hambye and M. H. G. Tytgat, *Electroweak symmetry breaking induced by dark matter*, *Phys. Lett.* **B659** (2008) 651–655, [[arXiv:0707.0633](#)].

- [36] P. Agrawal, E. M. Dolle, and C. A. Krenke, *Signals of Inert Doublet Dark Matter in Neutrino Telescopes*, *Phys. Rev.* **D79** (2009) 015015, [[arXiv:0811.1798](#)].
- [37] E. M. Dolle and S. Su, *The Inert Dark Matter*, *Phys. Rev.* **D80** (2009) 055012, [[arXiv:0906.1609](#)].
- [38] Q.-H. Cao, E. Ma, and G. Rajasekaran, *Observing the Dark Scalar Doublet and its Impact on the Standard-Model Higgs Boson at Colliders*, *Phys. Rev. D* **76** (2007) 095011, [[arXiv:0708.2939](#)].
- [39] L. Lopez Honorez, E. Nezri, J. F. Oliver, and M. H. G. Tytgat, *The Inert Doublet Model: An Archetype for Dark Matter*, *JCAP* **02** (2007) 028, [[hep-ph/0612275](#)].
- [40] A. Goudelis, B. Herrmann, and O. Stål, *Dark matter in the Inert Doublet Model after the discovery of a Higgs-like boson at the LHC*, *JHEP* **09** (2013) 106, [[arXiv:1303.3010](#)].
- [41] R. Barbieri, L. J. Hall, and V. S. Rychkov, *Improved naturalness with a heavy Higgs: An Alternative road to LHC physics*, *Phys. Rev.* **D74** (2006) 015007, [[hep-ph/0603188](#)].
- [42] E. Dolle, X. Miao, S. Su, and B. Thomas, *Dilepton Signals in the Inert Doublet Model*, *Phys. Rev.* **D81** (2010) 035003, [[arXiv:0909.3094](#)].
- [43] M. Aoki, S. Kanemura, and H. Yokoya, *Reconstruction of Inert Doublet Scalars at the International Linear Collider*, *Phys. Lett.* **B725** (2013) 302–309, [[arXiv:1303.6191](#)].
- [44] A. Arhrib, R. Benbrik, and N. Gaur, *$H \rightarrow \gamma\gamma$ in Inert Higgs Doublet Model*, *Phys. Rev.* **D85** (2012) 095021, [[arXiv:1201.2644](#)].
- [45] M. Krawczyk, D. Sokolowska, P. Swaczyna, and B. Swiezewska, *Constraining Inert Dark Matter by $R_{\gamma\gamma}$ and WMAP data*, *JHEP* **09** (2013) 055, [[arXiv:1305.6266](#)].
- [46] A. Arhrib, R. Benbrik, and T.-C. Yuan, *Associated Production of Higgs at Linear Collider in the Inert Higgs Doublet Model*, *Eur. Phys. J.* **C74** (2014) 2892, [[arXiv:1401.6698](#)].
- [47] A. Datta, N. Ganguly, N. Khan, and S. Rakshit, *Exploring collider signatures of the inert Higgs doublet model*, *Phys. Rev.* **D95** (2017), no. 1 015017, [[arXiv:1610.00648](#)].
- [48] B. Dutta, G. Palacio, J. D. Ruiz-Alvarez, and D. Restrepo, *Vector Boson Fusion in the Inert Doublet Model*, *Phys. Rev.* **D97** (2018), no. 5 055045, [[arXiv:1709.09796](#)].
- [49] J. Kalinowski, W. Kotlarski, T. Robens, D. Sokolowska, and A. F. Zarnecki, *Benchmarking the Inert Doublet Model for e^+e^- colliders*, *JHEP* **12** (2018) 081, [[arXiv:1809.07712](#)].
- [50] J. Kalinowski, W. Kotlarski, T. Robens, D. Sokolowska, and A. F. Zarnecki, *Exploring Inert Scalars at CLIC*, *JHEP* **07** (2019) 053, [[arXiv:1811.06952](#)].
- [51] Y. Guo-He, S. Mao, L. Gang, Z. Yu, and G. Jian-You, *Searches for dark matter via charged Higgs pair production in the Inert Doublet Model at $\gamma\gamma$ collider*, [arXiv:2006.06216](#).

- [52] F.-X. Yang, Z.-L. Han, and Y. Jin, *Same-Sign Dilepton Signature in the Inert Doublet Model*, [arXiv:2101.06862](#).
- [53] J. Kalinowski, T. Robens, D. Sokolowska, and A. F. Zarnecki, *IDM Benchmarks for the LHC and Future Colliders*, *Symmetry* **13** (2021), no. 6 991, [[arXiv:2012.14818](#)].
- [54] A. Melfo, M. Nemevsek, F. Nesti, G. Senjanovic, and Y. Zhang, *Inert Doublet Dark Matter and Mirror/Extra Families after Xenon100*, *Phys. Rev.* **D84** (2011) 034009, [[arXiv:1105.4611](#)].
- [55] D. Abercrombie et al., *Dark Matter Benchmark Models for Early LHC Run-2 Searches: Report of the ATLAS/CMS Dark Matter Forum*, *Phys. Dark Univ.* **27** (2020) 100371, [[arXiv:1507.00966](#)].
- [56] A. Ilnicka, M. Krawczyk, and T. Robens, *Inert Doublet Model in light of LHC Run I and astrophysical data*, *Phys. Rev. D* **93** (2016), no. 5 055026, [[arXiv:1508.01671](#)].
- [57] N. Blinov, J. Kozaczuk, D. E. Morrissey, and A. de la Puente, *Compressing the Inert Doublet Model*, *Phys. Rev. D* **93** (2016), no. 3 035020, [[arXiv:1510.08069](#)].
- [58] P. Poulose, S. Sahoo, and K. Sridhar, *Exploring the Inert Doublet Model through the dijet plus missing transverse energy channel at the LHC*, *Phys. Lett.* **B765** (2017) 300–306, [[arXiv:1604.03045](#)].
- [59] M. Hashemi and S. Najjari, *Observability of Inert Scalars at the LHC*, *Eur. Phys. J.* **C77** (2017), no. 9 592, [[arXiv:1611.07827](#)].
- [60] N. Wan, N. Li, B. Zhang, H. Yang, M.-F. Zhao, M. Song, G. Li, and J.-Y. Guo, *Searches for Dark Matter via Mono-W Production in Inert Doublet Model at the LHC*, *Commun. Theor. Phys.* **69** (2018), no. 5 617.
- [61] A. Belyaev, T. R. Fernandez Perez Tomei, P. G. Mercadante, C. S. Moon, S. Moretti, S. F. Novaes, L. Panizzi, F. Rojas, and M. Thomas, *Advancing LHC probes of dark matter from the inert two-Higgs-doublet model with the monojet signal*, *Phys. Rev.* **D99** (2019), no. 1 015011, [[arXiv:1809.00933](#)].
- [62] G. Belanger, B. Dumont, A. Goudelis, B. Herrmann, S. Kraml, and D. Sengupta, *Dilepton constraints in the Inert Doublet Model from Run 1 of the LHC*, *Phys. Rev.* **D91** (2015), no. 11 115011, [[arXiv:1503.07367](#)].
- [63] D. Dercks and T. Robens, *Constraining the Inert Doublet Model using Vector Boson Fusion*, *Eur. Phys. J.* **C79** (2019), no. 11 924, [[arXiv:1812.07913](#)].
- [64] Y.-L. S. Tsai, V. Q. Tran, and C.-T. Lu, *Confronting dark matter co-annihilation of Inert two Higgs Doublet Model with a compressed mass spectrum*, *JHEP* **06** (2020) 033, [[arXiv:1912.08875](#)].
- [65] G. Gil, P. Chankowski, and M. Krawczyk, *Inert Dark Matter and Strong Electroweak Phase Transition*, *Phys. Lett.* **B717** (2012) 396–402, [[arXiv:1207.0084](#)].
- [66] B. Swiezewska, *Inert scalars and vacuum metastability around the electroweak scale*, *JHEP* **07** (2015) 118, [[arXiv:1503.07078](#)].

- [67] N. Blinov, S. Profumo, and T. Stefaniak, *The Electroweak Phase Transition in the Inert Doublet Model*, *JCAP* **1507** (2015) 028, [[arXiv:1504.05949](#)].
- [68] F. P. Huang and J.-H. Yu, *Exploring inert dark matter blind spots with gravitational wave signatures*, *Phys. Rev.* **D98** (2018), no. 9 095022, [[arXiv:1704.04201](#)].
- [69] A. Belyaev, G. Cacciapaglia, I. P. Ivanov, F. Rojas-Abatte, and M. Thomas, *Anatomy of the Inert Two Higgs Doublet Model in the light of the LHC and non-LHC Dark Matter Searches*, *Phys. Rev.* **D97** (2018), no. 3 035011, [[arXiv:1612.00511](#)].
- [70] A. Arhrib, Y.-L. S. Tsai, Q. Yuan, and T.-C. Yuan, *An Updated Analysis of Inert Higgs Doublet Model in light of the Recent Results from LUX, PLANCK, AMS-02 and LHC*, *JCAP* **1406** (2014) 030, [[arXiv:1310.0358](#)].
- [71] B. Eiteneuer, A. Goudelis, and J. Heisig, *The inert doublet model in the light of Fermi-LAT gamma-ray data: a global fit analysis*, *Eur. Phys. J.* **C77** (2017), no. 9 624, [[arXiv:1705.01458](#)].
- [72] A. Ghosh, P. Konar, and S. Seth, *On precise probing of inert Higgs doublet model at the LHC*, [arXiv:2111.15236](#).
- [73] A. Jueid, J. Kim, S. Lee, S. Y. Shim, and J. Song, *Phenomenology of the Inert Doublet Model with a global $U(1)$ symmetry*, *Phys. Rev.* **D102** (2020), no. 7 075011, [[arXiv:2006.10263](#)].
- [74] M. Krawczyk, D. Sokołowska, P. Swaczyna, and B. Świeżewska, *Higgs $\rightarrow \gamma\gamma$, $Z\gamma$ in the Inert Doublet Model*, *Acta Phys. Polon.* **B44** (2013), no. 11 2163–2170, [[arXiv:1309.7880](#)].
- [75] R. Enberg, J. Rathsman, and G. Wouda, *Higgs properties in a broken Inert Doublet Model*, *JHEP* **08** (2013) 079, [[arXiv:1304.1714](#)]. [Erratum: JHEP01,087(2015)].
- [76] M. Krawczyk, D. Sokolowska, and B. Swiezewska, *Inert Doublet Model with a 125 GeV Higgs*, in *Proceedings, 1st Toyama International Workshop on Higgs as a Probe of New Physics 2013 (HPNP2013): Toyama, Japan, February 13-16, 2013*, 2013, [arXiv:1304.7757](#).
- [77] S. Kanemura, K. Mawatari, and K. Sakurai, *Single Higgs production in association with a photon at electron-positron colliders in extended Higgs models*, *Phys. Rev. D* **99** (2019), no. 3 035023, [[arXiv:1808.10268](#)].
- [78] M. Hashemi, M. Krawczyk, S. Najjari, and A. F. Żarnecki, *Production of Inert Scalars at the high energy e^+e^- colliders*, [arXiv:1512.01175](#). [JHEP02,187(2016)].
- [79] A. Ahriche, A. Arhrib, A. Jueid, S. Nasri, and A. de La Puente, *Mono-Higgs Signature in the Compressed scotogenic Model*, [arXiv:1811.00490](#).
- [80] A. Ilnicka, T. Robens, and T. Stefaniak, *Constraining Extended Scalar Sectors at the LHC and beyond*, *Mod. Phys. Lett. A* **33** (2018), no. 10n11 1830007, [[arXiv:1803.03594](#)].
- [81] M. Aiko, S. Kanemura, and K. Mawatari, *Exploring the global symmetry structure of the Higgs potential via same-sign pair production of charged Higgs bosons*, *Phys. Lett. B* **797** (2019) 134854, [[arXiv:1906.09101](#)].

- [82] A. Arhrib, K. Cheung, and C.-T. Lu, *Same-sign charged Higgs boson pair production in bosonic decay channels at the HL-LHC and HE-LHC*, *Phys. Rev. D* **102** (2020), no. 9 095026, [[arXiv:1910.02571](#)].
- [83] T. Han, S. Li, S. Su, W. Su, and Y. Wu, *Heavy Higgs bosons in 2HDM at a muon collider*, *Phys. Rev. D* **104** (2021), no. 5 055029, [[arXiv:2102.08386](#)].
- [84] A. G. Akeroyd, A. Arhrib, and C. Dove, *Charged and pseudoscalar higgs boson production at a muon collider*, *Phys. Rev. D* **61** (Feb, 2000) 071702.
- [85] H. Abouabid, A. Arhrib, R. Benbrik, J. El Falaki, B. Gong, W. Xie, and Q.-S. Yan, *One-loop radiative corrections to $e^+e^- \rightarrow Zh^0/H^0A^0$ in the Inert Higgs Doublet Model*, *JHEP* **05** (2021) 100, [[arXiv:2009.03250](#)].
- [86] M. Aiko, S. Kanemura, and K. Mawatari, *Next-to-leading-order corrections to the Higgs strahlung process from electron-positron collisions in extended Higgs models*, *Eur. Phys. J. C* **81** (2021), no. 11 1000, [[arXiv:2109.02884](#)].
- [87] M. J. Ramsey-Musolf, J.-H. Yu, and J. Zhou, *Probing extended scalar sectors with precision $e^+e^- \rightarrow Zh$ and Higgs diphoton studies*, *JHEP* **10** (2021) 155, [[arXiv:2104.10709](#)].
- [88] A. Arhrib, R. Benbrik, J. El Falaki, and A. Jueid, *Radiative corrections to the Triple Higgs Coupling in the Inert Higgs Doublet Model*, *JHEP* **12** (2015) 007, [[arXiv:1507.03630](#)].
- [89] S. Kanemura, M. Kikuchi, and K. Sakurai, *Testing the dark matter scenario in the inert doublet model by future precision measurements of the Higgs boson couplings*, *Phys. Rev. D* **94** (2016), no. 11 115011, [[arXiv:1605.08520](#)].
- [90] S. Banerjee, F. Boudjema, N. Chakrabarty, G. Chalons, and H. Sun, *Relic density of dark matter in the inert doublet model beyond leading order: The heavy mass case*, *Phys. Rev. D* **100** (2019), no. 9 095024, [[arXiv:1906.11269](#)].
- [91] S. Banerjee, F. Boudjema, N. Chakrabarty, and H. Sun, *Relic density of dark matter in the inert doublet model beyond leading order for the low mass region: 1. Renormalisation and constraints*, [arXiv:2101.02165](#).
- [92] S. Banerjee, F. Boudjema, N. Chakrabarty, and H. Sun, *Relic density of dark matter in the inert doublet model beyond leading order for the low mass region: 2. Co-annihilation*, [arXiv:2101.02166](#).
- [93] S. Banerjee, F. Boudjema, N. Chakrabarty, and H. Sun, *Relic density of dark matter in the inert doublet model beyond leading order for the low mass region: 3. Annihilation in 3-body final state*, [arXiv:2101.02167](#).
- [94] S. Banerjee, F. Boudjema, N. Chakrabarty, and H. Sun, *Relic density of dark matter in the inert doublet model beyond leading order for the low mass region: 4. The Higgs resonance region*, [arXiv:2101.02170](#).
- [95] S. Banerjee and N. Chakrabarty, *A revisit to scalar dark matter with radiative corrections*, *JHEP* **05** (2019) 150, [[arXiv:1612.01973](#)].

- [96] S. Kanemura, M. Kikuchi, K. Mawatari, K. Sakurai, and K. Yagyu, *Full next-to-leading-order calculations of Higgs boson decay rates in models with non-minimal scalar sectors*, *Nucl. Phys. B* **949** (2019) 114791, [[arXiv:1906.10070](#)].
- [97] J. Braathen and S. Kanemura, *Leading two-loop corrections to the Higgs boson self-couplings in models with extended scalar sectors*, *Eur. Phys. J. C* **80** (2020), no. 3 227, [[arXiv:1911.11507](#)].
- [98] J. Braathen and S. Kanemura, *On two-loop corrections to the Higgs trilinear coupling in models with extended scalar sectors*, *Phys. Lett. B* **796** (2019) 38–46, [[arXiv:1903.05417](#)].
- [99] E. Senaha, *Radiative Corrections to Triple Higgs Coupling and Electroweak Phase Transition: Beyond One-loop Analysis*, *Phys. Rev. D* **100** (2019), no. 5 055034, [[arXiv:1811.00336](#)].
- [100] A. Arhrib, M. Capdequi Peyranere, and G. Moultaka, *Fermion and Sfermion effects in e^+e^- charged Higgs pair production*, *Phys. Lett. B* **341** (1995) 313–324, [[hep-ph/9406357](#)].
- [101] M. A. Diaz and T. A. ter Veldhuis, *Radiative corrections to charged Higgs production in e^+e^- colliders*, in *1994 Meeting of the American Physical Society, Division of Particles and Fields (DPF 94)*, pp. 1116–1119, 1, 1995. [hep-ph/9501315](#).
- [102] A. Arhrib and G. Moultaka, *Radiative corrections to $e^+e^- \rightarrow H^+H^-$: THDM versus MSSM*, *Nucl. Phys. B* **558** (1999) 3–40, [[hep-ph/9808317](#)].
- [103] M. Beccaria, A. Ferrari, F. M. Renard, and C. Verzegnassi, *Complete electroweak one loop contributions to the pair production cross section of MSSM charged and neutral Higgs bosons in e^+e^- collisions*, [hep-ph/0506274](#).
- [104] M. Beccaria, F. M. Renard, S. Trimarchi, and C. Verzegnassi, *Charged Higgs production in the 1-TeV domain as a probe of supersymmetric models*, *Phys. Rev. D* **68** (2003) 035014, [[hep-ph/0212167](#)].
- [105] J. Guasch, W. Hollik, and A. Kraft, *Radiative corrections to pair production of charged Higgs bosons at TESLA*, in *2nd Workshop of the 2nd Joint ECFA / DESY Study on Physics and Detectors for a Linear Electron Positron Collider*, pp. 205–218, 10, 1999. [hep-ph/9911452](#).
- [106] J. Guasch, W. Hollik, and A. Kraft, *Radiative corrections to pair production of charged Higgs bosons in e^+e^- collisions*, *Nucl. Phys. B* **596** (2001) 66–80.
- [107] S. Heinemeyer and C. Schappacher, *Charged Higgs Boson production at e^+e^- colliders in the complex MSSM: a full one-loop analysis*, *Eur. Phys. J. C* **76** (2016), no. 10 535, [[arXiv:1606.06981](#)].
- [108] E. Lundstrom, M. Gustafsson, and J. Edsjo, *The Inert Doublet Model and LEP II Limits*, *Phys. Rev. D* **79** (2009) 035013, [[arXiv:0810.3924](#)].
- [109] A. Belyaev, U. Blumenschein, A. Freegard, S. Moretti, and D. Sengupta, *Multilepton signatures from dark matter at the LHC*, *JHEP* **09** (2022) 173, [[arXiv:2204.06411](#)].

- [110] T. Robens, *Investigating extended scalar sectors at current and future colliders*, *PoS LHCP2019* (2019) 138, [arXiv:1908.10809].
- [111] I. F. Ginzburg, K. A. Kanishev, M. Krawczyk, and D. Sokolowska, *Evolution of Universe to the present inert phase*, *Phys. Rev.* **D82** (2010) 123533, [arXiv:1009.4593].
- [112] B. W. Lee, C. Quigg, and H. B. Thacker, *Weak Interactions at Very High-Energies: The Role of the Higgs Boson Mass*, *Phys. Rev.* **D16** (1977) 1519.
- [113] P. M. Ferreira and B. Swiezewska, *One-loop contributions to neutral minima in the inert doublet model*, *JHEP* **04** (2016) 099, [arXiv:1511.02879].
- [114] V. Cacchio, D. Chowdhury, O. Eberhardt, and C. W. Murphy, *Next-to-leading order unitarity fits in Two-Higgs-Doublet models with soft \mathbb{Z}_2 breaking*, *JHEP* **11** (2016) 026, [arXiv:1609.01290].
- [115] **ATLAS** Collaboration, M. Aaboud et al., *Measurements of Higgs boson properties in the diphoton decay channel with 36 fb^{-1} of pp collision data at $\sqrt{s} = 13\text{ TeV}$ with the ATLAS detector*, *Phys. Rev. D* **98** (2018) 052005, [arXiv:1802.04146].
- [116] **CMS** Collaboration, A. M. Sirunyan et al., *Measurements of Higgs boson properties in the diphoton decay channel in proton-proton collisions at $\sqrt{s} = 13\text{ TeV}$* , *JHEP* **11** (2018) 185, [arXiv:1804.02716].
- [117] **ATLAS** Collaboration, *Combination of searches for invisible Higgs boson decays with the ATLAS experiment*, ATLAS-CONF-2020-052.
- [118] B. Swiezewska and M. Krawczyk, *Diphoton rate in the inert doublet model with a 125 GeV Higgs boson*, *Phys. Rev.* **D88** (2013), no. 3 035019, [arXiv:1212.4100].
- [119] M. E. Peskin and T. Takeuchi, *Estimation of oblique electroweak corrections*, *Phys. Rev.* **D46** (1992) 381–409.
- [120] **Particle Data Group** Collaboration, M. Tanabashi et al., *Review of Particle Physics*, *Phys. Rev.* **D98** (2018), no. 3 030001.
- [121] **Particle Data Group** Collaboration, P. A. Zyla et al., *Review of Particle Physics*, *PTEP* **2020** (2020), no. 8 083C01.
- [122] L. F. Abbott and P. Sikivie, *A Cosmological Bound on the Invisible Axion*, *Phys. Lett.* **120B** (1983) 133–136.
- [123] M. Dine and W. Fischler, *The Not So Harmless Axion*, *Phys. Lett.* **120B** (1983) 137–141.
- [124] J. Preskill, M. B. Wise, and F. Wilczek, *Cosmology of the Invisible Axion*, *Phys. Lett.* **120B** (1983) 127–132.
- [125] G. Belanger, A. Mjallal, and A. Pukhov, *Recasting direct detection limits within micrOMEGAs and implication for non-standard Dark Matter scenarios*, pre-print (3, 2020) [arXiv:2003.08621].
- [126] **XENON** Collaboration, E. Aprile et al., *Dark Matter Search Results from a One Ton-Year Exposure of XENON1T*, *Phys. Rev. Lett.* **121** (2018), no. 11 111302, [arXiv:1805.12562].

- [127] **PICO** Collaboration, C. Amole et al., *Dark Matter Search Results from the Complete Exposure of the PICO-60 C₃F₈ Bubble Chamber*, *Phys. Rev. D* **100** (2019), no. 2 022001, [arXiv:1902.04031].
- [128] **CRESST** Collaboration, A. H. Abdelhameed et al., *First results from the CRESST-III low-mass dark matter program*, *Phys. Rev. D* **100** (2019), no. 10 102002, [arXiv:1904.00498].
- [129] **DarkSide** Collaboration, P. Agnes et al., *Low-Mass Dark Matter Search with the DarkSide-50 Experiment*, *Phys. Rev. Lett.* **121** (2018), no. 8 081307, [arXiv:1802.06994].
- [130] **ATLAS** Collaboration, M. Aaboud et al., *Search for dark matter and other new phenomena in events with an energetic jet and large missing transverse momentum using the ATLAS detector*, *JHEP* **01** (2018) 126, [arXiv:1711.03301].
- [131] **CMS** Collaboration, A. M. Sirunyan et al., *Search for dark matter produced with an energetic jet or a hadronically decaying W or Z boson at $\sqrt{s} = 13$ TeV*, *JHEP* **07** (2017) 014, [arXiv:1703.01651].
- [132] M. Bohm, H. Spiesberger, and W. Hollik, *On the One Loop Renormalization of the Electroweak Standard Model and Its Application to Leptonic Processes*, *Fortsch. Phys.* **34** (1986) 687–751.
- [133] W. F. L. Hollik, *Radiative Corrections in the Standard Model and their Role for Precision Tests of the Electroweak Theory*, *Fortsch. Phys.* **38** (1990) 165–260.
- [134] A. Denner, *Techniques for calculation of electroweak radiative corrections at the one loop level and results for W physics at LEP-200*, *Fortsch. Phys.* **41** (1993) 307–420, [arXiv:0709.1075].
- [135] A. Denner and S. Dittmaier, *Electroweak Radiative Corrections for Collider Physics*, *Phys. Rept.* **864** (2020) 1–163, [arXiv:1912.06823].
- [136] A. Denner, L. Jenniches, J.-N. Lang, and C. Sturm, *Gauge-independent \overline{MS} renormalization in the 2HDM*, *JHEP* **09** (2016) 115, [arXiv:1607.07352].
- [137] A. Denner, S. Dittmaier, and J.-N. Lang, *Renormalization of mixing angles*, *JHEP* **11** (2018) 104, [arXiv:1808.03466].
- [138] M. Krause, R. Lorenz, M. Muhlleitner, R. Santos, and H. Ziesche, *Gauge-independent Renormalization of the 2-Higgs-Doublet Model*, *JHEP* **09** (2016) 143, [arXiv:1605.04853].
- [139] B. Harris and J. Owens, *The Two cutoff phase space slicing method*, *Phys. Rev. D* **65** (2002) 094032, [hep-ph/0102128].
- [140] W. Beenakker, S. C. van der Marck, and W. Hollik, *$e^+ e^-$ annihilation into heavy fermion pairs at high-energy colliders*, *Nucl. Phys. B* **365** (1991) 24–78.
- [141] V. S. Fadin, V. A. Khoze, and A. D. Martin, *On $W^+ W^-$ production near threshold*, *Phys. Lett. B* **311** (1993) 311–316.

- [142] D. Y. Bardin, W. Beenakker, and A. Denner, *The Coulomb singularity in off-shell W pair production*, *Phys. Lett. B* **317** (1993) 213–217.
- [143] A. Sommerfeld, *Über die Beugung und Bremsung der Elektronen*, *Annalen Phys.* **403** (1931), no. 3 257–330.
- [144] A. D. Sakharov, *Interaction of an Electron and Positron in Pair Production*, *Zh. Eksp. Teor. Fiz.* **18** (1948) 631–635.
- [145] T. Hahn, *Generating Feynman diagrams and amplitudes with FeynArts 3*, *Comput. Phys. Commun.* **140** (2001) 418–431, [[hep-ph/0012260](#)].
- [146] T. Hahn and M. Perez-Victoria, *Automatized one loop calculations in four-dimensions and D -dimensions*, *Comput. Phys. Commun.* **118** (1999) 153–165, [[hep-ph/9807565](#)].
- [147] T. Hahn and M. Rauch, *News from FormCalc and LoopTools*, *Nucl. Phys. Proc. Suppl.* **157** (2006) 236–240, [[hep-ph/0601248](#)]. [[236\(2006\)](#)].
- [148] T. Hahn, *Loop calculations with FeynArts, FormCalc, and LoopTools*, *Acta Phys. Polon.* **B30** (1999) 3469–3475, [[hep-ph/9910227](#)].
- [149] T. Hahn, *Feynman Diagram Calculations with FeynArts, FormCalc, and LoopTools*, *PoS ACAT2010* (2010) 078, [[arXiv:1006.2231](#)].
- [150] J.-X. Wang, *Progress in FDC project*, *Nucl. Instrum. Meth.* **A534** (2004) 241–245, [[hep-ph/0407058](#)].
- [151] S. Kawabata, *A New version of the multidimensional integration and event generation package BASES/SPRING*, *Comput. Phys. Commun.* **88** (1995) 309–326.
- [152] C. Degrande, *Automatic evaluation of UV and R_2 terms for beyond the Standard Model Lagrangians: a proof-of-principle*, *Comput. Phys. Commun.* **197** (2015) 239–262, [[arXiv:1406.3030](#)].
- [153] J. Heisig, S. Kraml, and A. Lessa, *Constraining new physics with searches for long-lived particles: Implementation into SModelS*, *Phys. Lett. B* **788** (2019) 87–95, [[arXiv:1808.05229](#)].
- [154] A. Belyaev, S. Prestel, F. Rojas-Abbate, and J. Zurita, *Probing dark matter with disappearing tracks at the LHC*, *Phys. Rev. D* **103** (2021), no. 9 095006, [[arXiv:2008.08581](#)].
- [155] **CEPC Study Group** Collaboration, M. Dong et al., *CEPC Conceptual Design Report: Volume 2 - Physics & Detector*, [arXiv:1811.10545](#).
- [156] Y. Tan et al., *Search for invisible decays of the Higgs boson produced at the CEPC*, *Chin. Phys. C* **44** (2020), no. 12 123001, [[arXiv:2001.05912](#)].
- [157] **LZ** Collaboration, J. Aalbers et al., *First Dark Matter Search Results from the LUX-ZEPLIN (LZ) Experiment*, [arXiv:2207.03764](#).
- [158] X. Mo, G. Li, M.-Q. Ruan, and X.-C. Lou, *Physics cross sections and event generation of e^+e^- annihilations at the CEPC*, *Chin. Phys. C* **40** (2016), no. 3 033001, [[arXiv:1505.01008](#)].

- [159] W. Kilian, T. Ohl, and J. Reuter, *WHIZARD: Simulating Multi-Particle Processes at LHC and ILC*, *Eur. Phys. J. C* **71** (2011) 1742, [[arXiv:0708.4233](#)].
- [160] W. Xie, R. Benbrik, A. Habjia, S. Taj, B. Gong, and Q.-S. Yan, *Signature of 2HDM at Higgs Factories*, *Phys. Rev. D* **103** (2021), no. 9 095030, [[arXiv:1812.02597](#)].
- [161] N. Chakrabarty, T. Han, Z. Liu, and B. Mukhopadhyaya, *Radiative Return for Heavy Higgs Boson at a Muon Collider*, *Phys. Rev. D* **91** (2015), no. 1 015008, [[arXiv:1408.5912](#)].
- [162] M. Karliner, M. Low, J. L. Rosner, and L.-T. Wang, *Radiative return capabilities of a high-energy, high-luminosity e^+e^- collider*, *Phys. Rev. D* **92** (2015), no. 3 035010, [[arXiv:1503.07209](#)].
- [163] M. Greco, T. Han, and Z. Liu, *ISR effects for resonant Higgs production at future lepton colliders*, *Phys. Lett. B* **763** (2016) 409–415, [[arXiv:1607.03210](#)].
- [164] E. A. Kuraev and V. S. Fadin, *On Radiative Corrections to e^+e^- Single Photon Annihilation at High-Energy*, *Sov. J. Nucl. Phys.* **41** (1985) 466–472. [*Yad. Fiz.*41,733(1985)].
- [165] B. Gong and J.-X. Wang, *Next-to-Leading-Order QCD Corrections to $e^+e^- \rightarrow J/\psi$ at the B Factories*, *Phys. Rev. Lett.* **102** (2009) 162003, [[arXiv:0901.0117](#)].
- [166] B. Gong, L.-P. Wan, J.-X. Wang, and H.-F. Zhang, *Polarization for Prompt J/ψ and $\psi(2s)$ Production at the Tevatron and LHC*, *Phys. Rev. Lett.* **110** (2013), no. 4 042002, [[arXiv:1205.6682](#)].
- [167] Q.-F. Sun, F. Feng, Y. Jia, and W.-L. Sang, *Mixed electroweak-QCD corrections to $e^+e^- \rightarrow HZ$ at Higgs factories*, *Phys. Rev. D* **96** (2017), no. 5 051301, [[arXiv:1609.03995](#)].
- [168] Y. Gong, Z. Li, X. Xu, L. L. Yang, and X. Zhao, *Mixed QCD-EW corrections for Higgs boson production at e^+e^- colliders*, *Phys. Rev. D* **95** (2017), no. 9 093003, [[arXiv:1609.03955](#)].